

# Abnormal morphology biases haematocrit distribution in tumour vasculature and contributes to heterogeneity in tissue oxygenation

Miguel O. Bernabeu<sup>a,1</sup>, Jakub Köry<sup>b,2</sup>, James A. Grogan<sup>b,2</sup>, Bostjan  
Markelc<sup>c,d,2</sup>, Albert Beardo<sup>a</sup>, Mayeul d’Avezac<sup>e</sup>, Jakob Kaeppler<sup>b</sup>,  
Nicholas Daly<sup>a</sup>, James Hetherington<sup>f,g</sup>, Timm Krüger<sup>h</sup>, Philip K. Maini<sup>b</sup>,  
Joe M. Pitt-Francis<sup>i</sup>, Ruth J. Muschel<sup>c</sup>, Tomás Alarcón<sup>j,k,3</sup>, and Helen M.  
Byrne<sup>b,3,1</sup>

<sup>a</sup>Centre for Medical Informatics, Usher Institute, The University of  
Edinburgh, Edinburgh, UK

<sup>b</sup>Mathematical Institute, University of Oxford, Oxford, UK

<sup>c</sup>Department of Oncology, University of Oxford, Oxford, UK

<sup>d</sup>Department of Experimental Oncology, Institute of Oncology,  
Ljubljana, Slovenia

<sup>e</sup>Research Software Development Group, Research IT Services,  
University College London, London, UK

<sup>f</sup>The Alan Turing Institute, London, UK

<sup>g</sup>Department of Computer Science, University College London, London,  
UK

<sup>h</sup>School of Engineering, Institute for Multiscale Thermofluids, The  
University of Edinburgh, Edinburgh, UK

<sup>i</sup>Department of Computer Science, University of Oxford, Oxford, UK

<sup>j</sup>Centre de Recerca Matemàtica, Barcelona, Spain

<sup>k</sup>ICREA, Pg. Lluís Companys 23, 08010 Barcelona, Spain

<sup>1</sup>Corresponding authors: miguel.bernabeu@ed.ac.uk,  
helen.byrne@maths.ox.ac.uk

<sup>2</sup>Equally contributing authors

<sup>3</sup>Equally contributing senior authors

September 23, 2019

## Abstract

Oxygen heterogeneity in solid tumours is recognised as a limiting factor for therapeutic efficacy. Vessel normalisation strategies, aimed at rescuing abnormal tumour vascular phenotypes and alleviating hypoxia, have the potential to improve tumour responses to treatments such as radiotherapy and chemotherapy. However, understanding how pathological blood vessel networks and oxygen transport are related remains limited. In this paper, we propose a novel source of oxygen heterogeneity in tumour tissue associated with the abnormal transport of red blood cells. We calculate average vessel lengths  $\bar{L}$  and diameters  $\bar{d}$  from tumour allografts of three cancer cell lines and observe a substantial reduction in the ratio  $\lambda = \bar{L}/\bar{d}$  compared to physiological conditions. Mathematical modelling reveals that small values of the ratio  $\lambda$  (*i.e.*  $\lambda < 6$ ) can bias haematocrit distribution in tumour vascular networks and drive heterogeneous oxygenation of tumour tissue. Finally, we show an increase in the value of  $\lambda$  in tumour vascular networks following treatment with the anti-angiogenic cancer agent DC101. Based on our findings, we propose a mechanism for oxygen normalisation associated with an increase in  $\lambda$  following treatment with anti-angiogenic drugs.

## 1 Introduction

Tissue oxygenation plays a crucial role in the growth and response to treatment of cancer. Indeed, well-oxygenated tumour regions respond to radiotherapy better than hypoxic or oxygen-deficient regions, by a factor of up to three [1, 2]. Further, the increased rates of proteomic and genomic modifications and clonal selection associated with anoxia (*i.e.*, total oxygen depletion), endow tumours with more aggressive and metastatic phenotypes [3, 4]. Oxygen heterogeneity in solid tumours is commonly attributed to their abnormal vasculature [5, 6]. Vessel normalisation strategies aimed at reducing tumour hypoxia [7] have been shown to improve survival in *e.g.* glioblastoma patients undergoing chemotherapy and/or radiotherapy [8].

The link between abnormal vascularisation and hypoxia is arguably multifactorial, including nonuniform vessel distribution, vessel non-perfusion, and issues with pressure gradients leading to slow flow or even its reversal. However, the dynamics of oxygen transport within whole tumour vascular networks have received only limited attention in the literature, *e.g.* [9, 10, 11]. Oxygen is transported through the vasculature by binding to haemoglobin in red blood cells (RBCs) [12]. Haematocrit, or the volume fraction of RBCs in whole blood, does not distribute uniformly at vessel bifurcations (*i.e.* branching points where three vessels meet) [13, 14]. At a bifurcation with one afferent and two efferent branches, it is typically assumed that the efferent branch with the highest flow rate will have the highest haematocrit [14, 15] due to, among other features, plasma-skimming caused by the presence of an RBC-depleted layer or cell free layer (CFL) [16]. Several theoretical models have been proposed to describe this effect *e.g.* [15, 17, 18]. Tumour vasculature is characterised by abnormal branching patterns, reduced average vessel lengths, and increased formation of arterio-venous shunts (see [19] for a review). While these changes can impact haematocrit splitting (HS), and tumour oxygenation, they have received little attention in the literature.

In this paper, we propose a novel source of oxygen heterogeneity in tumour tissue associated with the abnormal transport of RBCs. When we extract average vessel lengths  $\bar{L}$  and diameters  $\bar{d}$  from tumour allografts of three cancer cell lines we observe a substantial reduction in  $\lambda = \bar{L}/\bar{d}$ , an accepted parameter governing CFL dynamics, compared to physiological conditions. Detailed numerical simulations describing the transport of RBCs in plasma reveal: a) asymmetrical CFL width disruption following a bifurcation, and b) that the average measured  $\lambda$  value in tumour allografts is too small for the CFL to recover full symmetry between consecutive branching points leading to uneven haematocrit split in the downstream branching point. Further, the resulting bias in haematocrit distribution propagates and amplifies across multiple branching points. We argue that this memory effect can explain observations of haemoconcentration/haemodilution in tumour vasculature [9] and well perfused vessels that are hypoxic [10].

Based on the RBC simulations, we propose a new haematocrit splitting rule that accounts for CFL disruption due to pathologically small  $\lambda$  values. We integrate this rule into existing models of tumour blood flow and oxygen transport [20] and observe a haematocrit memory effect in densely branched vessel networks. As a consequence, the predicted tissue oxygenation is highly heterogeneous and differs markedly from predictions generated using rules for haematocrit splitting under physiological conditions (*e.g.* [21, 22, 23, 5, 24]). Finally, we demonstrate the clinical relevance of our findings by showing an increase in the average  $\lambda$  value of tumour vascular networks following treatment with the DC101 anti-angiogenic cancer agent. Based on our results, we postulate the existence of a tumour oxygen normalisation mechanism associated with an increase in the  $\lambda$  value after treatment with anti-angiogenic drugs. Future studies should elucidate its relative importance compared to established mechanisms of normalisation (*e.g.* permeability reduction, vessel decompression [25]).

## 2 Results

### 2.1 Average distance between vessel branch points is shorter in solid tumours than in healthy tissue

We implemented a protocol for *in vivo* imaging of tumour vasculature [26] and exploited our recently published methods for vessel segmentation [27, 28] and three-dimensional (3D) vascular network reconstruction to characterise the morphology of tumour vasculature (see Methods section for more details). Briefly, tumour allografts of three murine cancer cell lines (*i.e.* MC38, colorectal carcinoma; B16F10, melanoma; and LLC, Lewis lung carcinoma) were implanted in mice, controlled for size, and imaged through an abdominal window chamber using a multi-photon microscope over multiple days. The vascular networks in the 3D image stacks were segmented and the associated network skeletons and vessel diameters computed [27, 28]. Figure 1(a)-(b) shows the two-dimensional (2D) maximum projection of an example dataset along with a 2D projection of its segmentation and a close-in overlaying segmentation and skeletonisation. Vessel lengths ( $L$ ) and diameters ( $d$ ) in the networks followed a right-skewed distribution resembling a log-normal distribution (Figure 1(c)-(e)). No correlation was found between the variables (Pearson's  $r^2 < 0.04$  for all samples analysed, Figure 1(c)-(e), Supplementary Tables S4–S5).

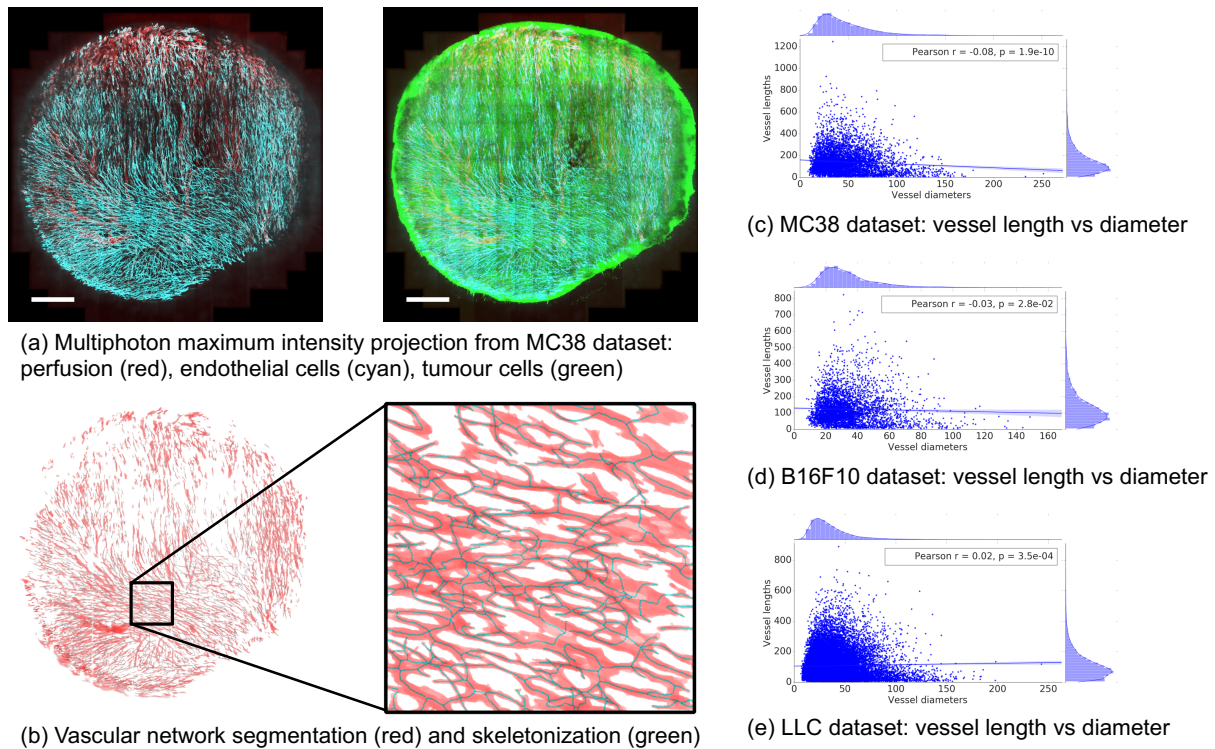


Figure 1: (a) Maximum intensity projection of multiphoton image stack of a tumour vessel network obtained via an abdominal imaging window in mouse. Red - perfusion, Cyan - endothelial cells, Green - GFP tumor cells. Scale bar: 1 mm. (b) The stack is subsequently segmented and skeletonised and distributions of vessel diameters and lengths are calculated. Mouse MC38-5 in Table 1. Scatter plots of vessel lengths versus diameters for different cell lines studied: (c) MC38 (Mouse 3 in Table 1), (d) B16F10 (Mouse 1 in Table 1), (e) LLC (Mouse 1 in Table 1).

Table 1 summarises last-day statistics for all the experiments and averages per cell line. In the example MC38 dataset from Figure 1(a), average vessel length ( $\bar{L}$ ) and diameter ( $\bar{d}$ ) were  $143 \mu\text{m}$  and  $45.5 \mu\text{m}$ , respectively. We observe how the group average vessel length is  $128.6 \mu\text{m}$ ,  $125.9 \mu\text{m}$ ,  $108.8 \mu\text{m}$  for MC38, B16F10, and LLC, respectively. The average diameters are  $33 \mu\text{m}$ ,  $36.5 \mu\text{m}$ ,  $35.7 \mu\text{m}$ , respectively, which is within the range previously described for tumour vasculature [29]. In addition, the length-to-diameter ratios ( $\lambda$ ) are 4.0, 3.4, 3.0, respectively, which is substantially smaller than typical  $\lambda$  values reported under physiological conditions in a variety of tissues (Supplementary Table S1) and representative of the high branching density encountered in tumour vasculature [19].

## 2.2 Plasma skimming in tumour-like vasculature is biased by history effects arising from cell free layer dynamics

Our finding of reduced inter branching point distance in tumour tissue motivated us to investigate a potential causal relationship between the reduction in  $L$  and  $\lambda$  and the profoundly abnormal tumour haemodynamics and mass transport patterns described

Table 1: Mean branch lengths ( $\bar{L}$ ), mean vessel diameters ( $\bar{d}$ ), and length-to-diameter ratio ( $\lambda = \frac{\bar{L}}{\bar{d}} = \frac{\sum L_i}{\sum d_i}$ ) measured over all the imaged vessels in tumour allografts from three murine cancer cell lines. See Supplementary Tables S4–S5 for correlation between variables.

Cell line	MC38						
Mouse	1	2	3	4	5	6	Av.
$\bar{L}, \mu\text{m}$	123.9	129.9	143	112.4	132.1	130.0	128.6
$\bar{d}, \mu\text{m}$	29.3	33.0	45.5	23.9	28.9	37.5	33.0
$\lambda = \bar{L}/\bar{d}$	4.2	3.9	3.1	4.7	4.6	3.4	4.0

Cell line	B16F10				LLC
Mouse	1	2	3	Av.	1
$\bar{L}, \mu\text{m}$	123.2	123.5	131.0	125.9	108.8
$\bar{d}, \mu\text{m}$	33.9	34.1	41.6	36.5	35.7
$\lambda = \bar{L}/\bar{d}$	3.6	3.6	3.1	3.4	3.0

in the literature [30]. Of particular interest is establishing whether haemorheological phenomena may contribute to tumour heterogeneity and hypoxia.

The presence of an RBC-depleted region adjacent to the vessel walls (*i.e.* the cell free layer (CFL)) is a key contributor to plasma skimming (PS) [14, 15, 16]. Previous studies have shown CFL disruption after microvascular bifurcations and found that the length required for CFL recovery,  $l_r$ , is in the region of 10 vessel diameters ( $d$ ) for  $d < 40\mu\text{m}$  [15],  $8 - 15d$  for  $d \in [20, 24]\mu\text{m}$  [31], and  $25d$  for  $d \in [10, 100]\mu\text{m}$  [32]. These values are substantially higher than the average  $\lambda$  values given in Table 1,  $\lambda < l_r$ , and therefore we expect that, on average, CFL symmetry will not recover between the branching points in the networks under study.

Motivated by these findings, we exploited recent advances in blood flow simulation methods by our group and others [33, 34, 35, 36] to investigate the link between CFL dynamics and PS in a tumour-inspired 3D microvascular network. Our intention is to understand the extent to which CFL disruption effects arising at a bifurcation affect haematocrit splitting in downstream bifurcations for small inter-bifurcation distances relevant to tumour vasculature (see Methods section for further details). Briefly, we define a set of networks of 3D cylindrical channels of constant radius, consisting of one main channel with an inlet and an outlet and two side branches, which define two consecutive bifurcations (Supplementary Figure S1). We consider inter-bifurcation distances of four and 25 channel diameters based on our tumour vascular network analysis and the largest of the CFL recovery distances reviewed earlier. We position the two side branches on the same side of the main channel or on opposite sides. A computational model of liquid-filled deformable particles (discocytes approximating the shape of an RBC) suspended in an ambient fluid is used to simulate blood flow in the networks, with RBCs inserted at the network inlet and removed at the outlets (see Materials and Methods and Supplementary Information for a summary of the simulation parameters). Flow rates at the network inlet and outlets are configured such that at each bifurcation flow is split evenly. We perform blood flow simulations (3 runs in each network, with random perturbations in the RBC insertion procedure) and, after the initial transient required to fully populate



the network with RBCs, we quantify haematocrit by an RBC-counting procedure.

Figure 2a–2b and Table 2 show how haematocrit split is close to even at bifurcation 1 for all geometries studied, as would be predicted by existing theoretical models of HS. However, different degrees of haematocrit splitting occur at bifurcation 2. In the double-t geometry, we observe haemodilution in branch 3 and haemoconcentration in branch 4 (16.8% vs 23%,  $p < 0.001$ , Figure 2b), which we will refer to as the unfavourable and favourable branches. These effects are not statistically significant in the same branches in the extended double-t geometry (19.1% vs 19.4%,  $p = 0.3$ , Figure 2a). The haemoconcentration/haemodilution effect is present in the cross geometry but the branches experiencing it are interchanged (22.1% vs 17.1%,  $p < 0.001$ , Figure 2c). In contrast with these results, existing HS theoretical models would predict even haematocrit splitting at bifurcation 2, regardless of the inter-bifurcation distance, due to the prescribed symmetrical flow and geometry conditions.

On closer inspection, the dynamics of the CFL show how, after bifurcation 1, CFL width is initially negligible and rapidly increases on the side of channel 1 leading to the favourable branch ( $\theta = 0$ , Figure 2f). Conversely, CFL width increases after the bifurcation and follows a downward trend in the opposite side ( $\theta = \pi$ , Figure 2f). An inter-bifurcation distance of four diameters is too short for the CFL width to equalise on both sides (Figures 2f). In contrast, CFL width has time to become symmetric on both sides for an inter-bifurcation distance of 25 diameters (Figure 2g).

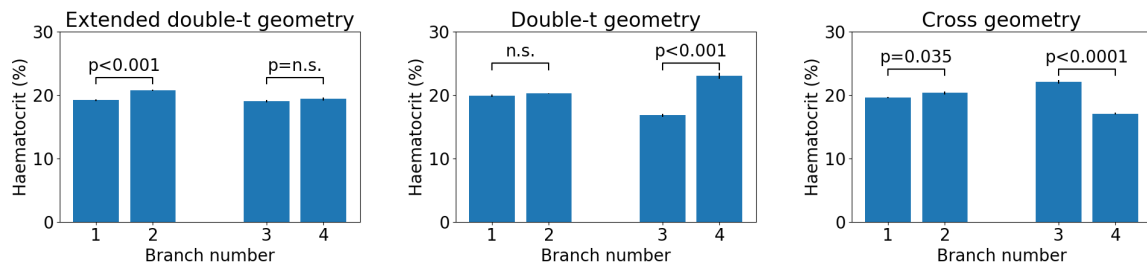
Taken together, these results show how CFL asymmetry can cause uneven haematocrit split in bifurcation 2 (Figure 2e) irrespective of branching side, *i.e.* cross *vs* double-t geometry. Our results are consistent with the findings by Pries *et al.*, describing how asymmetry of the haematocrit profile in the feeding vessel of a bifurcation has a significant influence on RBC distribution in the daughter vessels [15]. In addition, we provide quantitative evidence of how CFL asymmetry may be the main contributing factor.

Interestingly, we observe small but statistically significant asymmetries in the haematocrit split in bifurcation 1 in the extended double-t geometry (19.2% vs 20.8%,  $p < 0.001$ , Figure 2a) and cross geometry (19.7% vs 20.4%,  $p = 0.035$ , Figure 2c), which consistently favour the side branch. We attribute this secondary effect to an asymmetrical streamline split in the chosen geometry as investigated in [37].

We note that the effects described above depend on the angle between the planes containing the two consecutive bifurcations. Our data suggest that for angles of  $\frac{\pi}{2}$  radian the asymmetric haematocrit split effects will not be observed since the CFL width at  $\frac{\pi}{2}$  and  $\frac{3\pi}{2}$  remains mostly symmetric (Supplementary Figure S2).

### 2.3 Haematocrit history effects lead to highly heterogeneous oxygen distributions in solid tumours

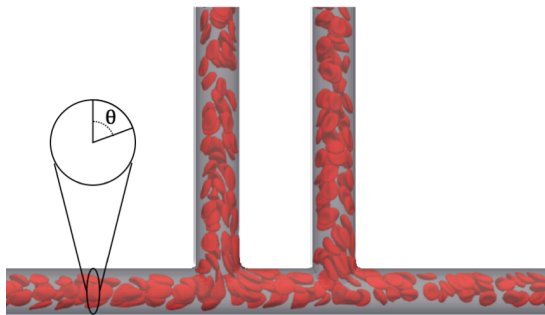
Existing theoretical models of haematocrit splitting (HS) [38, 18, 39] do not capture the haemoconcentration/haemodilution effects in the previous section. We hypothesise that this is because they neglect CFL disruption at bifurcations and its impact on subsequent bifurcations. We propose a new HS model which accounts for CFL dynamics and show that it predicts history effects in dense networks (see Materials and Methods section for details and Supplementary Information for a description of its validation). The new model is significantly less computationally intensive to solve than the RBC simulations



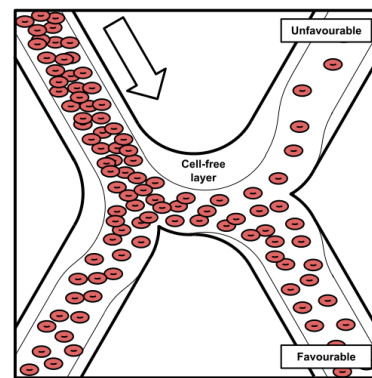
(a) Extended double-t geometry (see Suppl. Fig. S1a)

(b) Double-t geometry (see Suppl. Fig. S1b)

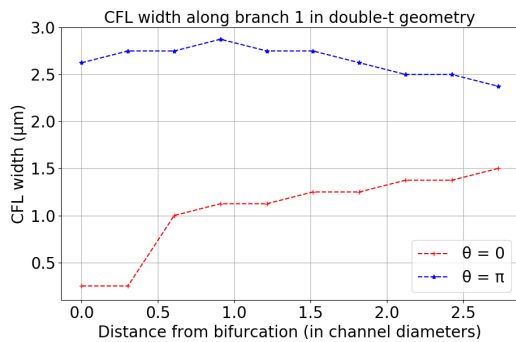
(c) Cross geometry (see Suppl. Fig. S1c)



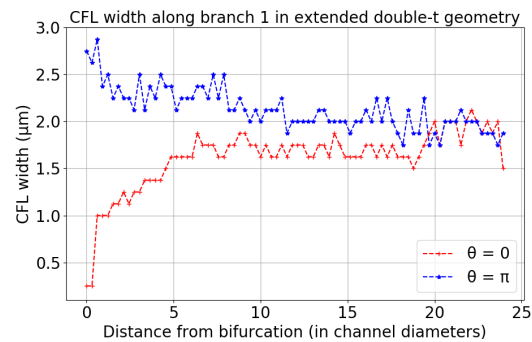
(d) Simulated RBCs in domain.



(e) Illustration of CFL dynamics and plasma skimming.



(f) CFL branch 1 (double-t geometry)



(g) CFL branch 1 (extended double-t geometry)

Figure 2: Haematocrit at different geometry branches (see Supplementary Figure S1 for geometry schematics): (a) extended double-t geometry, (b) double-t geometry, (c) cross geometry. Example simulation in the double-t geometry: (d) vessel network is rendered semi-transparent in grey, RBC membranes are rendered in red suspended in transparent blood plasma. (e) Schematic describing the impact of CFL dynamics on haematocrit split. CFL width in opposite sides of channel 1: (f) double-t geometry, (g) extended double-t geometry.

Table 2: Haematocrit calculated at the different branches of each bifurcation for the extended double-t (EDT) geometry, double-t (DT) geometry, and cross (X) geometry (see Supplementary Figure S1 for geometry schematics). Values are given as mean (standard error) over an ensemble of three simulations with random perturbations in the RBC insertion procedure while the haematocrit at the inlet is held constant.

	Bifurcation 1		
	Branch 0	Branch 1	Branch 2
EDT	20.06(0.03)	19.23(0.14)	20.8(0.1)
DT	20.08(0.06)	19.96(0.19)	20.26(0.05)
X	20.06(0.02)	19.67(0.09)	20.35(0.2)

	Bifurcation 2		
	Branch 1	Branch 3	Branch 4
EDT	19.23(0.14)	19.05(0.22)	19.4(0.23)
DT	19.96(0.19)	16.83(0.24)	23.04(0.46)
X	19.67(0.09)	22.12(0.26)	17.09(0.13)

(see Materials and Methods for details).

We use Murray’s law [40] and our experimentally measured values of  $\lambda$  to design a synthetic vessel network comprising consecutive double-t/cross bifurcations (see Supplementary Figure S4a and Materials and Methods for details). Most notably, at all bifurcations the flow split and the radii of the daughter vessels are equal, a scenario where existing HS models would predict homogeneous haematocrit throughout the network. We simulate network blood flow using a Poiseuille flow approximation with a HS model originally proposed by Pries *et al.* [15, 38] (without memory effects) and our new model (accounting for memory effects). As for the RBC simulations, differences in haematocrit between daughter branches emerge after two bifurcations (Supplementary Figure S4c), and are amplified with increasing vessel generation number (Supplementary Figure S4d).

Our model predicts the emergence of a compensatory mechanism in daughter branches. Increased flow resistance in the branch experiencing haemoconcentration leads to partial re-routing of flow in the other branch (Supplementary Figure S4b). This, in turn, attenuates the haemoconcentration/haemodilution effects previously described due to HS dependence on flow ratios.

We now consider how this memory effect in the haematocrit distribution may affect oxygen distribution in the tissue being perfused by the synthetic network. Following [20] (see Materials and Methods for a description of the coupled model), the haematocrit distribution in the network acts as a distributed source term in a reaction-diffusion equation for tissue oxygen. We define sink terms so that oxygen is consumed at a constant rate everywhere within the tissue. The equation is solved numerically and oxygen distributions generated using two HS models (with and without memory effects, Supplementary Figures S5a–S5b) are compared for a range of  $\lambda$  values. We focus on the central portion of the network (Figures 3a–3b) where the tissue is densely vascularised. The results presented in Figure 3c and Supplementary Figure S6 show that for larger values of  $\lambda$  the differences in the oxygen distribution in the tissue for the two HS models are not statistically significant (*e.g.* with  $\lambda = 10$ ,  $p = 0.14$ ). However, as  $\lambda$  decreases, statistically



significant differences appear (*e.g.* with  $\lambda = 4$ ,  $p < 0.001$ ). Without memory effects, the oxygen distributions become narrower as  $\lambda$  decreases; with memory effects, the oxygen distributions are increasingly wider for  $\lambda < 10$  (see Supplementary Figure S6c) leading to higher dispersion in the distributions for small  $\lambda$ . This is indicative of much more heterogeneous tissue oxygenation.

In the current study, we do not consider other sources of heterogeneity such as anisotropic transport and heterogeneous consumption of oxygen or other morphological abnormalities in the vascular networks. We hypothesise that their interaction with the haematocrit history effects reported here will further accentuate tissue oxygen heterogeneity.

## 2.4 Vascular normalisation therapies increase $\lambda$ ratio in tumours

Our findings of reduced  $\lambda$  ratio in tumour vasculature and associated predictions of increased oxygen heterogeneity led us to investigate whether existing vascular normalisation therapies modulate this parameter. Previous reports (Supplementary Table S2) have extensively demonstrated in multiple animal models that anti-angiogenic treatment leads to reduction in tumour vessel diameters. In those studies that analyse vessel length and diameter post-treatment, vessel length either remains unchanged or decreases to a lesser extent than vessel diameter. These findings indicate an increase in  $\lambda$  ratio post-treatment. Furthermore, Kamoun *et al.* also reported a reduction in tumour haemoconcentration post-treatment [41], which suggests an *in vivo* link between an increase in  $\lambda$ , haematocrit normalisation and oxygen transport homogenisation.

We validated these results in our animal model by calculating the  $\lambda$  ratio following DC101 treatment (see Materials and Methods for details). Our results indicate that in the first two days post-treatment  $\lambda$  increases significantly and then starts to decrease matching the control trend (Figure 4, Supplementary Table S3). This change is explained by a linear increase in vessel length immediately after treatment (absent in the control group), which is compensated after two days by an increase at a higher rate in vessel diameter (comparable to the control group) (Supplementary Figure S7).

## 3 Discussion

Hypoxia compromises the response of many tumours to treatments such as radiotherapy, chemotherapy and immunotherapy. Dominant causative factors for hypoxia associated with the structure and function of the tumour vasculature include tortuosity, immature blood vessels that are prone to collapse, and inadequate flow regulation. Motivated by morphological analyses of vascular networks from different tumour types and detailed computer simulations of RBC transport through synthetic networks, we have proposed a new, rheological mechanism for tumour hypoxia.

We analysed vascular networks from murine MC38, B16F10, and LLC tumour allografts. For each vessel segment within each network, we calculated a novel metric  $\lambda$  which is the ratio of its length and diameter. Average  $\lambda$  values for the three tumour cell lines were similar in magnitude ( $\bar{\lambda} \in [3, 4.2]$ ) and several fold smaller than values from a range of healthy tissues ( $\bar{\lambda} \in [9.5, 70]$ ). Detailed numerical simulations of RBC transport

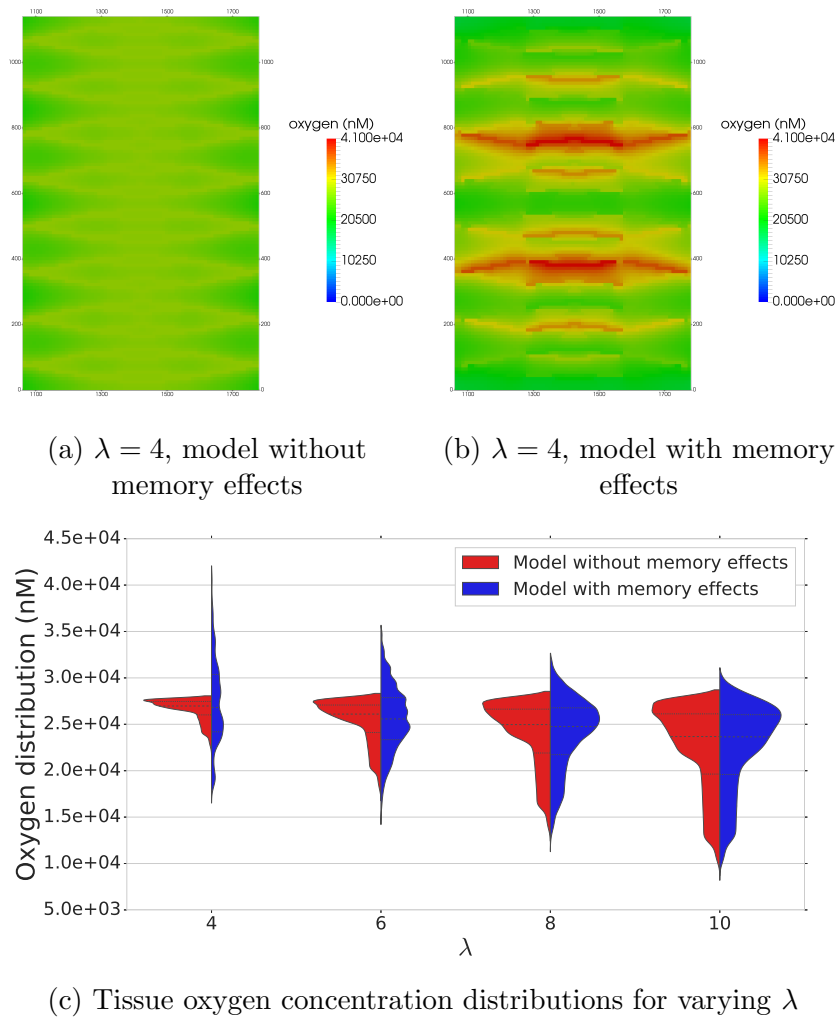


Figure 3: For  $\lambda = 4.0$ , the model with memory effects yields more pronounced oxygen heterogeneity (*i.e.* more dispersed oxygen distribution) in (a) and (b) (spatial scales are in microns). Violin plots in (c) show oxygen distributions for varying  $\lambda$  and the two HS models under consideration. Heterogeneity increases with  $\lambda$  for the model without memory effects as expected, but the model with memory effects predicts increased heterogeneity for very low  $\lambda$ . The horizontal lines in oxygen distributions in (c) represent 25, 50 and 75% percentiles.

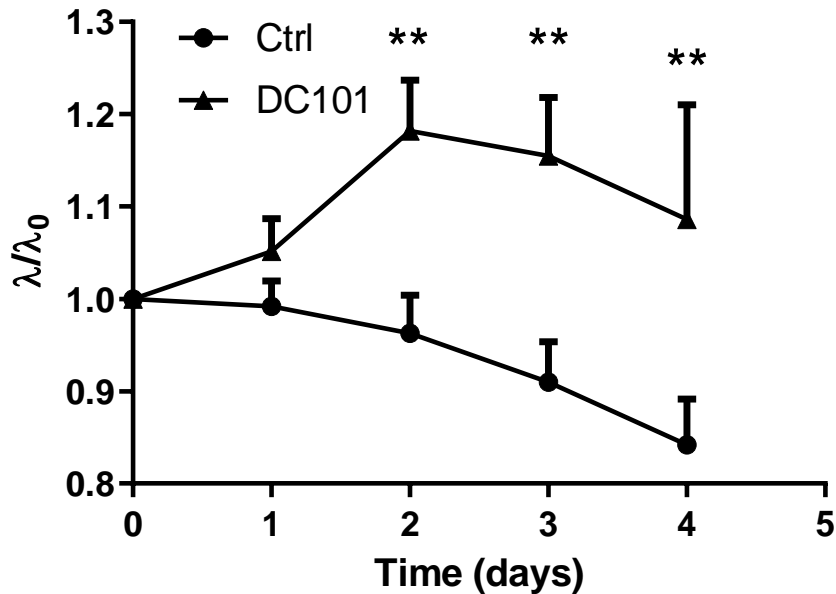


Figure 4:  $\lambda$  ratio in MC38 tumours over time following DC101 treatment compared with control (n=5). DC101 raw data is given in Supplementary Table S3. \*\*  $p < 0.01$ .

in plasma confirmed previous reports of transient alterations in the CFL downstream of network bifurcations (*e.g.* asymmetries in the cross-sectional haematocrit profile following a bifurcation [42, 43] and the temporal dynamics governing its axisymmetry recovery [32]). Further, for the  $\lambda$  values measured in our tumours and the capillary number considered in our simulations, the CFL did not become symmetric between consecutive branching points. This bias is amplified across branching points and drives haemoconcentration/haemodilution at the network level. Based on these findings, we developed a new rule for haematocrit splitting at vessel bifurcations that accounts for CFL disruption due to abnormally short vessel segments and validated it against our fully resolved RBC simulations. We then used our existing oxygen transport model [20] to demonstrate that this haematocrit memory effect can generate heterogeneous oxygen distributions in tissues perfused by highly branched vascular networks and that the network metric  $\lambda$  controls the extent of this heterogeneity. Finally, we reported an increase in the average  $\lambda$  value of tumour vascular networks following treatment with the DC101 anti-angiogenic cancer agent.

The implications of our findings are multiple. We have introduced a simple metric to characterise tumour vasculature based on the mean length-to-diameter ratio of vessel segments ( $\lambda$ ), and demonstrated how it controls oxygen heterogeneity in a synthetic, densely vascularised, tissue model. Our findings, of structurally induced haemodilution in vascular networks with low  $\lambda$  values, provide a mechanistic explanation for experimental observations of haemodilution in tumour vascular networks [9], the existence of well-perfused vessels that are hypoxic [10], and a possible explanation for the presence of cycling hypoxia in tumour microenvironment [44]. We conclude that vessel perfusion is a poor surrogate for oxygenation in tissue perfused by vascular networks with low  $\lambda$

values. Further, predictions of tissue oxygenation based on diffusion-dominated oxygen transport (*e.g.* [21, 22, 23, 5, 24]) may be inaccurate if they neglect heterogeneity in the haematocrit distribution of the vessel network.

Finally, anti-angiogenic drugs have been shown to generate transient periods of heightened homogeneous tissue oxygenation, due to improved restructuring and reduced permeability of tumour vessels [45]. This phenomenon, termed ‘vascular normalisation’ [6], can correct the deficient transport capabilities of tumour vasculature, homogenise drug and oxygen coverage, and, thereby, improve radiotherapy and chemotherapy effectiveness [2]. Based on our findings, we postulate the existence of a new oxygen normalisation mechanism associated with an increase in the average  $\lambda$  value of tumour vascular networks post treatment with anti-angiogenic drugs. Our results demonstrate how such morphological changes would lead to a less heterogeneous haematocrit distribution and more uniform intratumoural oxygenation. Further experimental work, quantifying haematocrit network dynamics before and after anti-angiogenic treatment, is needed to test this hypothesis and elucidate its importance in comparison with established mechanisms of normalisation (*e.g.* permeability reduction, vessel decompression [25]). If confirmed, this finding would provide a theoretical foundation for the development of therapeutic approaches for the normalisation of tumour oxygenation involving the administration of vascular targeting agents that normalise  $\lambda$  and, therefore, homogenise haematocrit and tissue oxygenation. Possible mechanisms to be targeted would include, among others, the promotion of post-angiogenic vascular remodelling [46, 47, 48], in particular vessel pruning and diameter control.

In summary, tissue oxygenation is central to cancer therapy. Understanding what controls tumour tissue oxygen concentration and transport is key to improving the efficacy of cancer treatments based on new and existing methods. Unravelling the causal relationship between vessel network structure and tissue oxygenation will pave the way for new therapies.

## 4 Materials and Methods

### 4.1 Tumour allograft model and abdominal imaging window protocol

We used an abdominal window chamber model in mice, which allowed for intravital imaging of the tumors [26]. The abdominal window chamber was surgically implanted in transgenic mice on C57Bl/6 background that had expression of red fluorescent protein tdTomato only in endothelial cells. The murine colon adenocarcinoma - MC38, murine melanoma - B16F10, and murine Lewis Lung Carcinoma – LLC tumors with expression of green fluorescent protein (GFP) in the cytoplasm were induced by injecting 5  $\mu$ l of dense cell suspension in a 50/50 mixture of saline and matrigel (Corning, NY, USA). For DC101 treatment, mice bearing MC38 tumors were treated with anti-mouse VEGFR2 antibody (clone DC101, 500  $\mu$ g/dose, 27 mg/kg, BioXCell) injected intraperitoneally on the first and fourth day of imaging. Prior to imaging we intravenously injected 100  $\mu$ l of Qtracker 705 Vascular Labels (Thermo Fisher Scientific, MA, USA) which is a blood-pool based labelling agent, thus allowing us to determine whether vessels were perfused or not.

Isoflurane inhalation anesthesia was used throughout the imaging, mice were kept on a heated stage and in a heated chamber and their breathing rate was monitored. Tumor images were acquired with Zeiss LSM 880 microscope (Carl Zeiss AG), connected to a Mai-Tai tunable laser (Newport Spectra Physics). We used an excitation wavelength of 940 nm and the emitted light was collected with Gallium Arsenide Phosphide (GaAsP) detectors through a 524–546 nm bandpass filter for GFP and a 562.5–587.5 nm bandpass filter for tdTomato and with a multi-alkali PMT detector through a 670–760 nm bandpass filter for Qtracker 705. A 20x water immersion objective with NA of 1.0 was used to acquire a Zstacks-TileScan with dimensions of 512x512 pixels in x and y, and approximately 70 planes in z. Voxel size was 5  $\mu\text{m}$  in the z direction and 0.83  $\mu\text{m}$  x 0.83  $\mu\text{m}$  in the x-y plane. Each tumor was covered by approximately 100 tiles. The morphological characteristics of tumor vasculature were obtained from the acquired images as previously described [27, 28]. All animal studies were performed in accordance with the Animals Scientific Procedures Act of 1986 (UK) and Committee on the Ethics of Animal Experiments of the University of Oxford.

## 4.2 RBC simulations in synthetic capillary networks

We define a set of networks of cylindrical channels of diameter  $d$ . An inlet channel of length  $25d$  (channel 0) bifurcates into two channels of length  $\delta$  and  $25d$  at  $\pi$  and  $\pi/2$  radians clockwise, respectively (channels 1 and 2). Channel 1 bifurcates into two channels of length  $25d$  at  $\pi$  and  $\alpha$  radians clockwise, respectively (channels 3 and 4). We consider the following configurations (Supplementary Figure S1): double-t geometry ( $\delta = 4d, \alpha = \pi/2$ ), cross geometry ( $\delta = 4d, \alpha = 3\pi/2$ ), and extended double-t geometry ( $\delta = 25d, \alpha = \pi/2$ ).

A model of liquid-filled elastic membranes (discocytes of 8  $\mu\text{m}$  diameter approximating the shape of an RBC) suspended in an ambient fluid is used to simulate blood flow in the networks. We use the fluid structure interaction (FSI) algorithm previously presented and validated by Krüger *et al.* [49], which is based on coupling the lattice Boltzmann method (LBM), finite element method (FEM), and immerse boundary method (IBM). The discocyte membranes are discretised into 500 triangles, which imposes a voxel size of 0.8 $\mu\text{m}$  on the regular grid used in the LBM simulation. The mechanical properties of the membrane are defined to achieve a capillary number (*i.e.* the ratio of viscous fluid stress acting on the membrane and a characteristic elastic membrane stress) of 0.1 in channel 0. The coupled algorithm is implemented in the HemeLB blood flow simulation software [50, 51] (<http://ccs.chem.ucl.ac.uk/hemelb>). Simulations ran on up to 456 cores of the ARCHER supercomputer taking 11–32 hours. See Supplementary Information for full details.

A constant flow rate of  $Q_0 = \bar{v}_{inlet}\pi d^2/4$  and a procedure for RBC insertion with tube haematocrit  $H_{inlet}$  is imposed at the network inlet. The outlet flow rates are set to  $Q_2 = Q_0/2$  and  $Q_{3,4} = Q_0/4$  to ensure an equal flow split at each bifurcation. RBCs are removed from the computational domain when they reach the end of any outlet channel. Supplementary Table S6 summarises the key parameters in the model. We performed blood flow simulations (3 runs in each network, with random perturbations in the RBC insertion procedure) and, after the initial transient required to fully populate the network with RBCs, we quantified haematocrit by an RBC-counting procedure.



### 4.3 Hybrid model for tissue oxygen perfusion that accounts for history effects in vascular networks

We first explain how our vascular networks are designed. Then, we describe how blood flow and haematocrit are determined. Next, we introduce the HS models and explain how CFL memory effects are incorporated and the resulting flow problem solved. We conclude by describing how the resulting haematocrit distribution is used to calculate oxygen perfusion in the surrounding tissue. The basic steps of our method are summarised in the flow chart in Supplementary Figure S3.

#### 4.3.1 Synthetic network design

Our networks have one inlet vessel (with imposed blood pressure and haematocrit; we call this generation 0), which splits into two daughter vessels (generation 1), which then split into two daughter vessels (generation 2), and so on until a prescribed (finite) number of generations is reached. This defines a sequence of consecutive double-t/cross bifurcations. Thereafter, the vessels converge symmetrically in pairs until a single outlet vessel is obtained (with imposed blood pressure). At every bifurcation, the diameters of the two daughter vessels are assumed to be equal and determined by appealing to Murray's law [40]. Using the same vessel diameters in all simulations, we vary vessel lengths, so that for all vessels in the network, the lengths equal the product of  $\lambda$  (which is fixed for a given network) and the vessel diameter. We focus on  $\lambda$ -values in the range measured in our tumours. We choose a synthetic network so that only  $\lambda$ -related effects (and not other morphological network characteristics) contribute to haemoconcentration/haemodilution. In future work, we will investigate the combined effect on tissue oxygenation of the HS model with memory effects and other tumour vascular characteristics.

#### 4.3.2 Blood flow and haematocrit splitting

**Network flow problem.** Tissue oxygenation depends on the haematocrit distribution in the vessel network perfusing the tissue. The haematocrit distribution depends on the blood flow rates. These rates are determined by analogy with Ohm's law for electric circuits, with the resistance to flow depending on the local haematocrit via the Fahraeus-Lindquist effect (for details, see Supplementary Information and [52]). The flow rates and haematocrit are coupled. We impose conservation of RBCs at all network nodes<sup>1</sup>. A HS rule must then be imposed at all diverging bifurcations.

**HS model without memory effects.** The empirical HS model proposed by Pries *et al.* [53] states that the volume fraction of RBCs entering a particular branch  $FQ_E$  depends on the fraction of the total blood flow entering that branch  $FQ_B$  as follows:

$$\text{logit}(FQ_E) = A + B \text{logit} \left( \frac{FQ_B - X_0}{1 - 2X_0} \right), \quad (1)$$

---

<sup>1</sup> $\sum_i \tilde{Q}_i H_i = 0$ , where we sum over all vessels  $i$  meeting at a given node with haematocrit  $H_i$  and signed flow rates  $\tilde{Q}_i$  (of magnitude  $Q_i$ ).

where  $\text{logit}(x) = \ln(x/(1-x))$ ,  $B$  serves to as a fitting parameter for the nonlinear relationship between  $FQ_E$  and  $FQ_B$ , and  $A$  introduces asymmetry between the daughter branches (note that for an equal flow split  $FQ_B = 0.5$ ,  $A \neq 0$  yields uneven splitting of haematocrit). Finally,  $X_0$  is the minimum flow fraction needed for RBCs to enter a particular branch (for lower flow fractions, no RBCs will enter)<sup>2</sup>; the term  $(1 - 2X_0)$  reflects the fact that the CFL exists in both daughter vessels (see Supplementary Figure S8a).

**HS model with memory effects.** We account for the effects of CFL disruption and recovery by modifying the parameters  $A$  and  $X_0$  (as already observed in [15]). For simplicity, and in the absence of suitable data, we assume that the parameter  $B$  is the same in both daughter branches. If  $X_{0,f}$  ( $A_f$ ) and  $X_{0,u}$  ( $A_u$ ) denote the values of  $X_0$  ( $A$ ) in the favourable and unfavourable daughter branches (see Figure 2e), then our new model of HS can be written as:

$$\text{logit}(FQ_{E,f}) = A_f + B \text{logit}\left(\frac{FQ_{B,f} - X_{0,f}}{1 - X_{0,u} - X_{0,f}}\right), \quad (2)$$

where subscripts  $f$  and  $u$  relate to favourable and unfavourable branches, respectively (see Supplementary Figure S8a for a graphical depiction). It is possible to rewrite (2) in terms of the suspension flow rates  $Q \equiv Q_B$  and haematocrit levels  $H$  of the favourable  $f$ , unfavourable  $u$ , and parent  $P$  vessels as (for details see Supplementary Information):

$$\frac{H_f}{H_u} = e^{A_f} \times \left(\frac{Q_f - X_{0,f}Q_P}{Q_u - X_{0,u}Q_P}\right)^B \times \frac{Q_u}{Q_f}. \quad (3)$$

This formulation of our HS model facilitates comparison with other HS models [17, 18, 39]. Functional forms for  $A_f$ ,  $X_{0,f}$  and  $X_{0,u}$  are based on our RBC simulation results and the existing literature (see Supplementary Information). We use an iterative scheme (as in [18]) to determine the flow rates and haematocrit in a given network.

### 4.3.3 Calculating the tissue oxygen distribution

We embed the vessel network in a rectangular tissue domain. A steady state reaction-diffusion equation models the tissue oxygen distribution, with source terms at vessel network locations proportional to the haematocrit there, and sink terms proportional to the local oxygen concentration modelling oxygen consumption by the tissue. This equation is solved numerically using Microvessel Chaste (see [20] and Supplementary Information for details). In order to highlight the influence of HS on tissue oxygen, we focus on the central 25% of the domain which is well-perfused and ignore the avascular corner regions (see Supplementary Figures S5a and S5b)

## Acknowledgements

We acknowledge HZ Ford for the cartoon in Figure 2e, the contributions of the HemeLB development team, and CD Arvanitis and V Vavourakis for helpful comments. Soft-

<sup>2</sup>The dependences of  $A$ ,  $B$  and  $X_0$  on the diameters of the participating vessels and on the parent vessel haematocrit are described in Supplementary Information, see (S.14)-(S.16).

ware development was supported by the Engineering and Physical Sciences Research Council (EPSRC) (grant eCSE-001-010). Supercomputing time on the ARCHER UK National Supercomputing Service (<http://www.archer.ac.uk>) was provided by the “UK Consortium on Mesoscale Engineering Sciences (UKCOMES)” under the EPSRC Grant No. EP/R029598/1. T.K.’s and M.O.B’s contribution have been funded through two Chancellor’s Fellowship at The University of Edinburgh. M.O.B is supported by grants from EPSRC (EP/R029598/1, EP/R021600/1), Fondation Leducq (17 CVD 03), and the European Union’s Horizon 2020 research and innovation programme under grant agreement No 801423. The research leading to these results has received funding from the People Programme (Marie Curie Actions) of the European Unions Seventh Framework Programme (FP7/2007- 2013) under REA grant agreement No 625631 (obtained by BM). This work was also supported by Cancer Research UK (CR-UK) grant numbers C5255/A18085 and C5255/A15935, through the CRUK Oxford Centre. This work was supported by the Biotechnology and Biological Sciences Research Council UK Multi-Scale Biology Network, grant number BB/M025888/1. We would like to acknowledge funding from the UK Fluids Network (EPSRC grant number EP/N032861/1) for a Short Research Visit between the Edinburgh and Oxford teams.

## References

- [1] J. A. Bertout, S. A. Patel, M. C. Simon, The impact of O<sub>2</sub> availability on human cancer. *Nature Reviews Cancer* **8**, 967–975 (2008).
- [2] L. H. Gray, A. D. Conger, M. Ebert, S. Hornsey, O. C. A. Scott, The Concentration of Oxygen Dissolved in Tissues at the Time of Irradiation as a Factor in Radiotherapy. *The British Journal of Radiology* **26**, 638–648 (1953).
- [3] N. S. Vasudev, A. R. Reynolds, Anti-angiogenic therapy for cancer: Current progress, unresolved questions and future directions. *Angiogenesis* **17**, 471–494 (2014).
- [4] A. L. Harris, Hypoxia — a key regulatory factor in tumour growth. *Nature Reviews Cancer* **2**, 38 (2002).
- [5] D. R. Grimes, P. Kannan, B. Markelc, R. Bates, R. J. Muschel, M. Partridge, Estimating oxygen distribution from vasculature in three-dimensional tumor tissue. *Journal of The Royal Society Interface* **13** (2016).
- [6] R. K. Jain, Normalization of tumor vasculature: an emerging concept in antiangiogenic therapy. *Science* **307**, 58–62 (2005).
- [7] R. K. Jain, Normalizing tumor vasculature with anti-angiogenic therapy: A new paradigm for combination therapy. *Nature Medicine* **7**, 987–989 (2001).
- [8] T. T. Batchelor, E. R. Gerstner, K. E. Emblem, D. G. Duda, J. Kalpathy-Cramer, M. Snuderl, M. Ancukiewicz, P. Polaskova, M. C. Pinho, D. Jennings, S. R. Plotkin, A. S. Chi, A. F. Eichler, J. Dietrich, F. H. Hochberg, C. Lu-Emerson, A. J. Iafrate, S. P. Ivy, B. R. Rosen, J. S. Loeffler, P. Y. Wen, A. G. Sorensen, R. K. Jain, Improved tumor oxygenation and survival in glioblastoma patients who show increased blood

- perfusion after cediranib and chemoradiation. *Proceedings of the National Academy of Sciences* **110**, 19059–19064 (2013).
- [9] W. S. Kamoun, S.-S. Chae, D. A. Lacorre, J. A. Tyrrell, M. Mitre, M. A. Gillissen, D. Fukumura, R. K. Jain, L. L. Munn, Simultaneous measurement of RBC velocity, flux, hematocrit and shear rate in vascular networks. *Nature Methods* **7**, 655–660 (2010).
- [10] G. Helmlinger, F. Yuan, M. Dellian, R. K. Jain, Interstitial pH and pO<sub>2</sub> gradients in solid tumors in vivo: High-resolution measurements reveal a lack of correlation. *Nature Medicine* **3**, 177–182 (1997).
- [11] M. Lee, A. Downes, Y.-Y. Chau, B. Serrels, N. Hastie, A. Elfick, V. Brunton, M. Frame, A. Serrels, In vivo imaging of the tumor and its associated microenvironment using combined CARS / 2-photon microscopy. *IntraVital* **4**, e1055430 (2015).
- [12] A. S. Popel, Theory of Oxygen Transport To Tissue. *Critical Reviews in Biomedical Engineering* **17**, 257–321 (1989).
- [13] K. Svanes, B. W. Zweifach, Variations in small blood vessel hematocrits produced in hypothermic rats by micro-occlusion. *Microvascular Research* **1**, 210–220 (1968).
- [14] Y. C. Fung, Stochastic flow in capillary blood vessels. *Microvascular Research* **5**, 34–48 (1973).
- [15] A. Pries, K. Ley, M. Claassen, P. Gaehtgens, Red cell distribution at microvascular bifurcations. *Microvascular Research* **38**, 81–101 (1989).
- [16] V. Doyeux, T. Podgorski, S. Peponas, M. Ismail, G. Coupier, Spheres in the vicinity of a bifurcation: Elucidating the Zweifach-Fung effect. *Journal of Fluid Mechanics* **674**, 359–388 (2011).
- [17] Y. C. Fung, *Biomechanics : Circulation* (Springer New York, 1997).
- [18] I. G. Gould, A. A. Linninger, Hematocrit Distribution and Tissue Oxygenation in Large Microcirculatory Networks. *Microcirculation* **22**, 1–18 (2015).
- [19] D. Ribatti, B. Nico, E. Crivellato, A. Vacca, The structure of the vascular network of tumors. *Cancer Letters* **248**, 18–23 (2007).
- [20] J. A. Grogan, A. J. Connor, B. Markelc, R. J. Muschel, P. K. Maini, H. M. Byrne, J. M. Pitt-Francis, Microvessel Chaste: An Open Library for Spatial Modeling of Vascularized Tissues. *Biophysical Journal* **112**, 1767–1772 (2017).
- [21] L. Hlatky, Clinical Application of Antiangiogenic Therapy: Microvessel Density, What It Does and Doesn't Tell Us. *CancerSpectrum Knowledge Environment* **94**, 883–893 (2002).
- [22] A. Daşu, I. Toma-Daşu, M. Karlsson, The effects of hypoxia on the theoretical modelling of tumour control probability. *Acta Oncologica* **44**, 563–571 (2005).

- [23] J. G. Scott, A. G. Fletcher, A. R. Anderson, P. K. Maini, Spatial Metrics of Tumour Vascular Organisation Predict Radiation Efficacy in a Computational Model. *PLoS Computational Biology* **12**, 1–24 (2016).
- [24] J. A. Grogan, B. Markelc, A. J. Connor, R. J. Muschel, J. M. Pitt-Francis, P. K. Maini, H. M. Byrne, Predicting the influence of microvascular structure on tumour response to radiotherapy. *IEEE Transactions on Biomedical Engineering* **PP** (2016).
- [25] T. Stylianopoulos, R. K. Jain, Combining two strategies to improve perfusion and drug delivery in solid tumors. *Proceedings of the National Academy of Sciences* **110**, 18632–18637 (2013).
- [26] L. Ritsma, E. J. Steller, S. I. Ellenbroek, O. Kranenburg, I. H. Borel Rinkes, J. Van Rheenen, Surgical implantation of an abdominal imaging window for intravital microscopy. *Nature Protocols* **8**, 583–594 (2013).
- [27] R. Bates, B. Irving, B. Markelc, J. Kaeppler, G. Brown, R. J. Muschel, S. M. Brady, V. Grau, J. A. Schnabel, Segmentation of Vasculature from Fluorescently Labeled Endothelial Cells in Multi-Photon Microscopy Images. *IEEE Transactions on Medical Imaging* pp. 1–10 (2017).
- [28] R. Bates, B. Irving, B. Markelc, J. Kaeppler, R. Muschel, V. Grau, J. A. Schnabel, Extracting 3D Vascular Structures from Microscopy Images using Convolutional Recurrent Networks. *arXiv:1705.09597* (2017).
- [29] S. J. Chapman, R. J. Shipley, R. Jawad, Multiscale modeling of fluid transport in tumors. *Bulletin of Mathematical Biology* **70**, 2334–2357 (2008).
- [30] F. Yuan, H. A. Salehi, Y. Boucher, R. K. Jain, U. S. Vasthare, R. F. Tuma, Vascular Permeability and Microcirculation of Gliomas and Mammary Carcinomas Transplanted in Rat and Mouse Cranial Windows. *Cancer Research* **54**, 4564–4568 (1994).
- [31] O. Oulaid, J. Zhang, Cell-free layer development process in the entrance region of microvessels. *Biomechanics and Modeling in Mechanobiology* **14**, 783–794 (2015).
- [32] D. Katanov, G. Gompper, D. A. Fedosov, Microvascular blood flow resistance: Role of red blood cell migration and dispersion. *Microvascular Research* **99**, 57–66 (2015).
- [33] T. Krüger, *Computer simulation study of collective phenomena in dense suspensions of red blood cells under shear* (Springer Spektrum, 2012).
- [34] P. Balogh, P. Bagchi, A computational approach to modeling cellular-scale blood flow in complex geometry. *Journal of Computational Physics* **334**, 280–307 (2017).
- [35] G. Závodszy, B. van Rooij, V. Azizi, A. Hoekstra, Cellular Level In-silico Modeling of Blood Rheology with An Improved Material Model for Red Blood Cells. *Frontiers in Physiology* **8**, 563 (2017).
- [36] D. A. Fedosov, B. Caswell, G. E. Karniadakis, A multiscale red blood cell model with accurate mechanics, rheology,dynamics. *Biophysical Journal* **98**, 2215–2225 (2010).



- [37] Z. Wang, Y. Sui, A. V. Salsac, D. Barthès-Biesel, W. Wang, Path selection of a spherical capsule in a microfluidic branched channel: Towards the design of an enrichment device. *Journal of Fluid Mechanics* **849**, 136–162 (2018).
- [38] A. R. Pries, T. W. Secomb, Microvascular blood viscosity in vivo and the endothelial surface layer. *American Journal of Physiology-Heart and Circulatory Physiology* **289**, H2657-H2664 (2005).
- [39] J. Yang, S. S. Yoo, T.-R. Lee, Effect of fractional blood flow on plasma skimming in the microvasculature. *Physical Review E* **95**, 040401 (2017).
- [40] C. D. Murray, The Physiological Principle of Minimum Work: I. The Vascular System and the Cost of Blood Volume. *Proceedings of the National Academy of Sciences* **12**, 207–214 (1926).
- [41] W. S. Kamoun, C. D. Ley, C. T. Farrar, A. M. Duyverman, J. Lahdenranta, D. A. Lacorre, T. T. Batchelor, E. Di Tomaso, D. G. Duda, L. L. Munn, D. Fukumura, A. Gregory Sorensen, R. K. Jain, Edema control by cediranib, a vascular endothelial growth factor receptor - Targeted kinase inhibitor, prolongs survival despite persistent brain tumor growth in mice. *Journal of Clinical Oncology* **27**, 2542–2552 (2009).
- [42] S. Kim, R. L. Kong, A. S. Popel, M. Intaglietta, P. C. Johnson, Temporal and spatial variations of cell-free layer width in arterioles. *American Journal of Physiology-Heart and Circulatory Physiology* **293**, H1526-H1535 (2007).
- [43] P. Balogh, P. Bagchi, The cell-free layer in simulated microvascular networks. *Journal of Fluid Mechanics* **864**, 768–806 (2019).
- [44] C. Michiels, C. Tellier, O. Feron, Biochimica et Biophysica Acta Cycling hypoxia : A key feature of the tumor microenvironment. *BBA - Reviews on Cancer* **1866**, 76–86 (2016).
- [45] R. T. Tong, Y. Boucher, S. V. Kozin, F. Winkler, D. J. Hicklin, R. K. Jain, Vascular normalization by vascular endothelial growth factor receptor 2 blockade induces a pressure gradient across the vasculature and improves drug penetration in tumors. *Cancer Research* **64**, 3731–3736 (2004).
- [46] C. A. Franco, M. L. Jones, M. O. Bernabeu, I. Geudens, T. Mathivet, A. Rosa, F. M. Lopes, A. P. Lima, A. Ragab, R. T. Collins, L.-K. Phng, P. V. Coveney, H. Gerhardt, Dynamic Endothelial Cell Rearrangements Drive Developmental Vessel Regression. *PLOS Biology* **13**, e1002125 (2015).
- [47] C. A. Franco, M. L. Jones, M. O. Bernabeu, A.-C. Vion, P. Barbacena, J. Fan, T. Mathivet, C. G. Fonseca, A. Ragab, T. P. Yamaguchi, P. V. Coveney, R. A. Lang, H. Gerhardt, Non-canonical Wnt signalling modulates the endothelial shear stress flow sensor in vascular remodelling. *eLife* **5** (2016).

- [48] A.-C. Vion, S. Alt, A. Klaus-Bergmann, A. Szymborska, T. Zheng, T. Perovic, A. Hammoutene, M. B. Oliveira, E. Bartels-Klein, I. Hollfinger, P.-E. Rautou, M. O. Bernabeu, H. Gerhardt, Primary cilia sensitize endothelial cells to BMP and prevent excessive vascular regression. *Journal of Cell Biology* **217**, 1651–1665 (2018).
- [49] T. Krüger, F. Varnik, D. Raabe, Efficient and accurate simulations of deformable particles immersed in a fluid using a combined immersed boundary lattice Boltzmann finite element method. *Computers and Mathematics with Applications* **61**, 3485–3505 (2011).
- [50] M. D. Mazzeo, P. V. Coveney, HemeLB: A high performance parallel lattice-Boltzmann code for large scale fluid flow in complex geometries. *Computer Physics Communications* **178**, 894–914 (2008).
- [51] M. O. Bernabeu, M. L. Jones, J. H. Nielsen, T. Krüger, R. W. Nash, D. Groen, S. Schmieschek, J. Hetherington, H. Gerhardt, C. A. Franco, P. V. Coveney, Computer simulations reveal complex distribution of haemodynamic forces in a mouse retina model of angiogenesis. *Journal of The Royal Society Interface* **11**, 20140543–20140543 (2014).
- [52] T. W. Secomb, Hemodynamics. *Comprehensive Physiology* **6**, 975–1003 (2016).
- [53] A. R. Pries, T. W. Secomb, P. Gaehtgens, J. F. Gross, Blood flow in microvascular networks. Experiments and simulation. *Circulation Research* **67**, 826–34 (1990).
- [54] Z. Guo, C. Zheng, B. Shi, Discrete lattice effects on the forcing term in the lattice Boltzmann method. *Physical Review E - Statistical, Nonlinear, and Soft Matter Physics* **65**, 1–6 (2002).
- [55] M. Bouzidi, M. Firdaouss, P. Lallemand, Momentum transfer of a Boltzmann-lattice fluid with boundaries. *Physics of Fluids* **13**, 3452 (2001).
- [56] A. J. C. Ladd, Numerical simulations of particulate suspensions via a discretized Boltzmann equation. Part 1. Theoretical foundation. *Journal of Fluid Mechanics* **271**, 285 (1994).
- [57] C. K. Aidun, J. R. Clausen, Lattice-Boltzmann Method for Complex Flows. *Annual Review of Fluid Mechanics* **42**, 439–472 (2010).
- [58] T. Krüger, H. Kusumaatmaja, A. Kuzmin, O. Shardt, G. Silva, E. M. Viggien, *The Lattice Boltzmann Method: Principles and Practice* (2017).
- [59] R. Skalak, P. I. Branemark, Deformation of Red Blood Cells in Capillaries. *Science* **164**, 717–719 (1969).
- [60] C. S. Peskin, *Acta Numerica*, A. Iserles, ed. (Cambridge University Press, Cambridge, 2002), vol. 11, pp. 479–518.
- [61] G. Gompper, M. Schick, *Soft Matter: Lipid bilayers and red blood cells* (Wiley, 2008).

- [62] A. R. Pries, T. W. Secomb, T. Gessner, M. B. Sperandio, J. F. Gross, P. Gaehtgens, Resistance to blood flow in microvessels in vivo. *Circulation Research* **75**, 904–915 (1994).
- [63] T. Alarcón, H. M. Byrne, P. K. Maini, A cellular automaton model for tumour growth in inhomogeneous environment. *Journal of Theoretical Biology* **225**, 257–274 (2003).
- [64] T. W. Secomb, R. Hsu, E. Y. H. Park, M. W. Dewhirst, Green 's Function Methods for Analysis of Oxygen Delivery to Tissue by Microvascular Networks. *Annals of biomedical engineering* **32**, 1519–1529 (2004).
- [65] B. R. Duling, I. H. Sarelius, W. F. Jackson, A comparison of microvascular estimates of capillary blood flow with direct measurements of total striated muscle flow. *International journal of microcirculation, clinical and experimental* **1**, 409–24 (1982).
- [66] A. S. Popel, A Model of Pressure and Flow Distribution in Branching Networks. *Journal of Applied Mechanics* **47**, 247 (1980).
- [67] M. P. Wiedeman, Lengths and Diameters of Peripheral Arterial Vessels in the Living Animal. *Circulation Research* **10**, 686–690 (1962).
- [68] M. P. Wiedeman, Dimensions of Blood Vessels from Distributing Artery to Collecting Vein. *Circulation Research* **12**, 375–378 (1963).
- [69] A. Koller, B. Dawant, A. Liu, A. S. Popel, P. C. Johnson, Quantitative analysis of arteriolar network architecture in cat sartorius muscle. *American Journal of Physiology-Heart and Circulatory Physiology* **253**, H154-H164 (1987).
- [70] S. D. House, P. C. Johnson, Diameter and blood flow of skeletal muscle venules during local flow regulation. *American Journal of Physiology-Heart and Circulatory Physiology* **250**, H828-H837 (1986).
- [71] M. Ellsworth, A. Liu, B. Dawant, A. Popel, R. Pittman, Analysis of vascular pattern and dimensions in arteriolar networks of the retractor muscle in young hamsters. *Microvascular Research* **34**, 168–183 (1987).
- [72] A. R. Pries, T. W. Secomb, Rheology of the microcirculation. *Clinical Hemorheology and Microcirculation* **29**, 143–8 (2003).
- [73] Y. Izumi, L. Xu, E. di Tomaso, D. Fukumura, R. K. Jain, Herceptin acts as an anti-angiogenic cocktail. *Nature* **416**, 279–280 (2002).
- [74] R. K. Jain, N. Safabakhsh, A. Sckell, Y. Chen, P. Jiang, L. Benjamin, F. Yuan, E. Keshet, Endothelial cell death, angiogenesis, and microvascular function after castration in an androgen-dependent tumor: role of vascular endothelial growth factor. *Proceedings of the National Academy of Sciences of the United States of America* **95**, 10820–5 (1998).

- [75] L. Primo, G. Seano, C. Roca, F. Maione, P. A. Gagliardi, R. Sessa, M. Martinelli, E. Giraudo, L. Di Blasio, F. Bussolino, Increased expression of  $\alpha 6$  integrin in endothelial cells unveils a proangiogenic role for basement membrane. *Cancer Research* **70**, 5759–5769 (2010).
- [76] F. Yuan, Y. Chen, M. Dellian, N. Safabakhsh, N. Ferrara, R. K. Jain, Time-dependent vascular regression and permeability changes in established human tumor xenografts induced by an anti-vascular endothelial growth factor/vascular permeability factor antibody. *Proceedings of the National Academy of Sciences* **93**, 14765–14770 (1996).
- [77] M. R. Owen, I. J. Stamper, M. Muthana, G. W. Richardson, J. Dobson, C. E. Lewis, H. M. Byrne, Mathematical modeling predicts synergistic antitumor effects of combining a macrophage-based, hypoxia-targeted gene therapy with chemotherapy. *Cancer Research* **71**, 2826–2837 (2011).
- [78] H. N. S. Michael J. Moran, *Fundamentals of Engineering Thermodynamics* (2006).
- [79] A. R. Pries, T. W. Secomb, P. Gaehtgens, Biophysical aspects of blood flow in the microvasculature. *Cardiovascular research* **32**, 654–67 (1996).

## A Supplementary information

The Supplementary Information is organised as follows. First, we provide experimental evidence which supports the findings that vessel lengths and diameters are uncorrelated in tumour environments. Next, we describe the fluid structure interaction (FSI) algorithm used for the red blood cell (RBC) simulations and the method used to calculate the width of the cell free layer (CFL). Next, we present our hybrid model of tissue perfusion and introduce our new haematocritic splitting (HS) model. Finally, we comment on the higher mean oxygen values predicted by our oxygen perfusion model for small  $\lambda$  values.

### A.1 Vessel lengths and diameters in tumour microvasculature are uncorrelated

In Supplementary Tables S4 and S5 we list Pearson’s  $r$ -values quantifying the correlation between vessel lengths,  $L$ , and diameters,  $d$ ,

$$\rho_{L,d} = \frac{\text{cov}(L, d)}{\sigma_L \sigma_d}, \quad (\text{S.1})$$

where  $\text{cov}(i, j)$  is the covariance of two variables and  $\sigma_i$  is the standard deviation of variable  $i$ , for the three tumour cell lines used in our experiments. Results are presented for each mouse and each scan. Day 0 was chosen as the day when the tumour vascular network appeared to be fully formed. This typically occurred approximately 8 days after tumour induction, when the tumour size was approximately 4mm in diameter. We note also that the duration of the observation period is cell-line specific; some tumours grew faster than others and, as a result, soon started pushing on the window, and in such cases the animal had to be culled as per licence limitations. The Pearson’s  $r$ -values are too low to conclude that a correlation exists between  $L$  and  $d$  in the tumour vascular networks studied.

### A.2 Red blood cell suspension model

The lattice Boltzmann method (LBM) numerically approximates the solution of the Navier-Stokes equations for a weakly compressible Newtonian fluid discretised on a regular lattice. We employ the D3Q19 lattice, the Bhatnagar–Gross–Krook collision operator extended with the Guo forcing scheme [54], the Bouzidi–Firdaouss–Lallemand (BFL) implementation of the no-slip boundary condition at the walls [55], and the Ladd implementation of the velocity boundary condition for open boundaries [56]. These methods have been extensively used and analysed in the literature (see [57, 58] for a detailed description).

The RBC membrane is modelled as a hyperelastic, isotropic and homogeneous material, following the model described in [33]. The total membrane energy  $W$  is defined by  $W = W^S + W^B + W^A + W^V$ , where the superscripts denote energy contributions due to strain, bending, area and volume. We employ the surface strain energy density  $w^S$



proposed by Skalak *et al.* [59]:

$$w^S = \frac{\kappa_s}{12} (I_1^2 + 2I_1 - 2I_2) + \frac{\kappa_\alpha}{12} I_2^2, \quad (\text{S.2})$$

$$I_1 = \lambda_1^2 + \lambda_2^2 - 2, \quad (\text{S.3})$$

$$I_2 = \lambda_1^2 \lambda_2^2 - 1, \quad (\text{S.4})$$

where  $\kappa_s$  and  $\kappa_\alpha$  are the shear and dilation moduli,  $\lambda_1, \lambda_2$  are the local principal in-plane stretch ratios (see [49] for calculation procedure), and  $W^S = \int dA w^S$ . The shape of the discocyte membrane is approximated by a number  $N_f$  of flat triangular faces, and  $W^S$  is numerically calculated based on a finite element method (FEM) approach as

$$W^S = \sum_{j=1}^{N_f} A_j^{(0)} w_j^s, \quad (\text{S.5})$$

where  $A_j^{(0)}$  is the undeformed area of face  $j$ . The bending energy of the RBC membrane is numerically calculated as

$$W^B = \sqrt{3} \kappa_B \sum_{\langle i,j \rangle} \left( \theta_{i,j} - \theta_{i,j}^{(0)} \right)^2, \quad (\text{S.6})$$

where  $\kappa_B$  is the bending modulus,  $\theta_{i,j}$  is the angle between the normals of two neighbouring faces  $i$  and  $j$ , and  $\theta_{i,j}^{(0)}$  is the same angle for the undeformed membrane. Finally, we penalise deviations of the total membrane surface area and volume by defining two additional energy contributions:

$$W^A = \frac{\kappa_A}{2} \frac{(A - A^{(0)})^2}{A^{(0)}}, \quad (\text{S.7})$$

$$W^V = \frac{\kappa_V}{2} \frac{(V - V^{(0)})^2}{V^{(0)}}, \quad (\text{S.8})$$

where  $\kappa_A, \kappa_V$  are the surface area and volume moduli,  $A$  and  $A^{(0)}$  are the current and undeformed membrane surface areas, and similarly with  $V$ . The principle of virtual work yields the force acting on each membrane vertex  $i$  at position  $\vec{x}_i$  through

$$\vec{F}_i = - \frac{\partial W(\{\vec{x}_i\})}{\partial \vec{x}_i}. \quad (\text{S.9})$$

The immersed boundary method [60] is used to couple the fluid and membrane dynamics. The fluid velocity is interpolated at the positions  $\vec{x}_i$  of the RBC mesh vertices, and a forward-Euler scheme is used to advect the vertices to satisfy the no-slip condition. The vertex forces  $\vec{F}_i$  are spread to the lattice where they are used as input to the forcing term in the LBM, which ensures local momentum exchange between the membrane and the fluid. See [33] for a detailed numerical analysis of the algorithm.

The RBC model contains five parameters ( $\kappa_s, \kappa_\alpha, \kappa_B, \kappa_A$ , and  $\kappa_V$ ). While  $\kappa_s$  and  $\kappa_B$  are known from experiments (see review in [61]), the exact values of the three remaining parameters are chosen to ensure that local area, total surface area and volume drift are constrained within a few percent and simulations are stable (see analysis in [33, 49]). Table S7 summarises all the parameters in the model.

### A.3 CFL width calculation

To calculate the CFL width in channel 1 of the domains in Supplementary Figure S1, let us consider a vessel cross-section of diameter  $d$  at distance  $l$  downstream from the first bifurcation in the network. The RBC density,  $\phi(r, \theta, l, t)$ , is 1 if there is a RBC at time  $t$  occupying the point with radial coordinate  $r$  and angular coordinate  $\theta$  of the cross-section and 0 otherwise. The average RBC density flux  $\Phi(l)$  going through the cross-section is

$$\Phi(l) = \frac{1}{N} \sum_{i=1}^N \int_0^{2\pi} d\theta \int_0^{d/2} r dr \phi(r, \theta, l, t_i) \mathbf{v}(r, \theta, l, t_i) \cdot \mathbf{n},$$

where  $\mathbf{v}$  is the fluid velocity,  $\mathbf{n}$  is the cross-section normal vector and  $N$  is the number of simulation time steps in the average (0.5 s of real time simulation sampled every 0.0215 s,  $N = 23$ , in our case).

We define  $\chi = 0.01$  as the average fraction of RBC density flux crossing the CFL. Now we are able to numerically determine the local CFL width  $W(l, \theta)$ : consider a 2D-cone centered and contained in the cross-section with orientation  $\theta$  and size  $\Delta\theta = \pi/2$ . The width  $W(l, \theta)$  is the distance such that

$$\chi = \frac{4}{\Phi N} \sum_{i=1}^N \int_{\theta-\Delta\theta/2}^{\theta+\Delta\theta/2} d\theta' \int_{d/2-W}^{d/2} r dr \phi(r, \theta', l, t_i) \mathbf{v}(r, \theta', l, t_i) \cdot \mathbf{n}.$$

Since we are only interested in the spatial evolution of the CFL, the specific value of  $\chi$  used in the definition is arbitrary. The choice of  $\chi$  will change the width of the CFL after symmetry recovery, but it will not affect the local characterisation of the CFL spatial evolution after a bifurcation. For example, for any value of  $\chi$ , the CFL recovery distance can be calculated as the shortest distance  $l$  for which the CFL width  $W$  do not depend on coordinate  $\theta$ .

### A.4 Hybrid model of oxygen transport in vascularised tissue

#### A.4.1 Choice of vessel diameters and branching angles in vascular networks

In the branched networks used, we fix the diameter of the inlet vessel so that  $d_{inlet} = 100 \mu\text{m}$ . The diameters of the two daughter vessels ( $d_\alpha$  and  $d_\beta$ ) are assumed to be equal and determined from the diameter of the parent vessel ( $d_P$ ) via Murray's law [40] so that:

$$d_P^3 = d_\alpha^3 + d_\beta^3 \equiv 2d_\alpha^3,$$

in which case

$$d_\alpha = \frac{d_P}{2^{1/3}}.$$

Since the network is symmetric about its central axis, vessels on the converging side have the same diameters as those of the same generation on the diverging side (see Supplementary Figure S4a). For all simulations the networks have 6 generations of vessels. The length  $L$  of a vessel segment in a given network is related to its diameter  $d$  via  $L = \lambda d$ , where the positive constant  $\lambda$  is network-specific.

For complete specification of the network geometry, in two-dimensional cartesian geometry, it remains to embed the network in a spatial domain. This is achieved by specifying

either the branching angles, or (equivalently) the lengths of the projections of the vessels on the  $y$  axis. Denoting by  $L_1^{vert}$  the length of the projection of a vessel of generation 1, the lengths of the projections of vessels of generation  $i > 1$  are given by  $L_i^{vert} = \frac{1}{2}L_{i-1}^{vert}$ . As a result, the vertical size of the domain will not exceed  $4L_1^{vert}$  for any number of generations. Finally, we require  $L_1^{vert} < L_1 =$  length of vessels of generation 1. In our simulations, we fix  $L_1^{vert} = 0.9L_1$  to ensure adequate spatial extent in the  $y$ - direction.

#### A.4.2 Poiseuille's law and the Fahraeus-Lindquist effect

We simulate flow in the branched networks by following the approach of Pries *et al.* [53]. For blood vessels of length  $L$  and diameter  $d$ , we assume Poiseuille's law

$$Q = \frac{\pi}{128} \frac{\Delta p d^4}{L \mu}, \quad (\text{S.10})$$

where  $Q$  is the vessel flow rate,  $\Delta p$  is the pressure drop along the vessel and  $\mu$  is the viscosity of blood [52]. Following [62] we assume that the blood viscosity depends on vessel diameter and haematocrit via the empirical relationship:

$$\mu = \mu_p \left[ 1 + (\mu_{45} - 1) \frac{(1 - H)^C - 1}{(1 - 0.45)^C - 1} \left( \frac{d}{d - 1.1} \right)^2 \right] \left[ \frac{d}{d - 1.1} \right]^2,$$

where  $\mu_p$  is the plasma viscosity,  $H$  is the vessel haematocrit,

$$\mu_{45} = 6e^{-0.085d} + 3.2 - 2.44e^{-0.06d^{0.645}}$$

and

$$C = (0.8 + e^{-0.075d}) \left( -1 + \frac{1}{1 + 10^{-11}d^{12}} \right) + \frac{1}{1 + 10^{-11}d^{12}}.$$

Introducing signed flow rates  $\tilde{Q}_i$  for the sake of brevity, we impose conservation of blood and haematocrit at each network bifurcation, so that

$$\sum_i \tilde{Q}_i = 0, \quad (\text{S.11})$$

and

$$\sum_i \tilde{Q}_i H_i = 0. \quad (\text{S.12})$$

In (S.11) and (S.12) we sum over the three vessels that meet at that bifurcation. At diverging bifurcations, we impose a HS rule: we use (1) from the main text when CFL memory effects are neglected and (2) from the main text when they are included. Denoting by  $N_B$  the number of network bifurcations and  $N_V$  the number of vessels, we have  $N_B$  unknown pressures  $P$ ,  $N_V$  unknown flow rates  $Q$  and  $N_V - 1$  unknown haematocrit levels (the inlet haematocrit being prescribed) - altogether  $N_B + 2N_V - 1$  unknowns. At the same time, we impose Poiseuille's law ((S.10)) for every vessel ( $N_V$  times), conservation of blood ((S.11)) and haematocrit ((S.12)) at every bifurcation node ( $N_B$  times), and an HS rule at all diverging bifurcations ( $N_B/2$  times), yielding a total of  $N_V + 5N_B/2$  algebraic equations. Since every bifurcation connects 3 vessels, we have  $N_V = (3N_B + 2)/2$ , where every vessel is counted twice, except for the inlet and outlet vessels (+2 in the numerator). From this, it follows that the number of equations ( $N_V + 5N_B/2$ ) equals the number of unknowns ( $N_B + 2N_V - 1$ ).

### A.4.3 Oxygen distribution in tissue

In this section, we determine the oxygen concentration  $c$  in the tissue. Following [20], we assume that the dominant processes governing its distribution are delivery from the vessel network (via one-way coupling with (S.12) and the haematocrit models (1) or (2), *i.e.*  $c$  depends on  $H_l$  but not vice versa), diffusive transport through the tissue, and consumption by cells in the tissue. We focus on the long time behaviour and, therefore, adopt a quasi-steady state approximation [63]

$$\underbrace{D\nabla^2 c}_{\text{diffusive transport through the tissue}} + \underbrace{\pi d_l \gamma \left( \frac{\beta_{ref}}{H_{ref}} H_l - c \right) \delta_{network}}_{\text{delivery from the blood vessels}} - \underbrace{\kappa c}_{\text{consumption by the tissue}} = 0. \quad (\text{S.13})$$

In (S.13), the positive constants  $D$ ,  $\gamma$  and  $\kappa$  represent the diffusion coefficient for oxygen in the tissue, the vessel permeability to oxygen, and the rate at which it is consumed by cells in the tissue. The vessel network is represented by a collection of Dirac point sources  $\delta_{network}$  where

$$\delta_{network}(\mathbf{x}) = \begin{cases} 1 & \text{if vessel is located at } \mathbf{x} \\ 0 & \text{otherwise} \end{cases}$$

and for any  $\mathbf{x}$  satisfying  $\delta_{network}(\mathbf{x}) = 1$ ,  $d_l$  and  $H_l$  are the diameter and haematocrit of the vessel at that location (where the latter has been calculated as described in the previous section). The constant  $\beta_{ref}$  represents the oxygen concentration of a reference vessel containing haematocrit  $H_{ref}$  (here we fix  $H_{ref} = 0.45$ , the inlet haematocrit) and we suppose that the oxygen concentration of a vessel with haematocrit  $H_l$  is  $\beta_{ref} H_l / H_{ref}$ . In (S.13) we assume that the oxygen is supplied by vessels to the tissue at a rate which is proportional to their circumference  $\pi d_l$ , the vessel permeability  $\gamma$ , and  $\beta_{ref} H_l / H_{ref} - c$ . Finally, we have  $\beta_{ref} = c_{stp} p_{ref} \alpha_{eff}$ , where  $c_{stp}$  denotes an ideal gas concentration at standard temperature and pressure,  $p_{ref}$  denotes the reference partial pressure at the inlet vessel, and  $\alpha_{eff}$  denotes the volumetric oxygen solubility [64]. A summary of the parameter values used to solve (S.13) is presented in Supplementary Table S8.

## A.5 Derivation of, and justification for, the HS model with CFL memory

### A.5.1 Parameter dependencies in HS model without memory from [38]

The dependencies of the parameters  $A$ ,  $B$  and  $X_0$  (see (1) from the main text) on the diameters of the parent and daughter vessels ( $d_P$ ,  $d_\alpha$  and  $d_\beta$ , respectively), and the discharge haematocrit  $H_P$  in the parent vessel were first introduced in [53] and later adjusted in [38] to achieve a better approximation under extreme combinations of  $d_\alpha$ ,  $d_\beta$ ,  $d_P$  and  $H_P$ . We will use the functional forms from [38], which read

$$A = -13.29 \left[ (d_\alpha^2 / d_\beta^2 - 1) / (d_\alpha^2 / d_\beta^2 + 1) \right] (1 - H_P) / d_P, \quad (\text{S.14})$$

$$B = 1 + 6.98 \left( \frac{1 - H_P}{d_P} \right) \quad (\text{S.15})$$

and

$$X_0 = 0.964(1 - H_P)/d_P. \quad (\text{S.16})$$

These functional forms assume that  $d_P$  is dimensionless and given by  $d_P = \frac{\hat{d}_P}{1\mu\text{m}}$ , where  $\hat{d}_P$  is the dimensional diameter. We maintain this convention throughout this section.

### A.5.2 HS model with memory

**Simplifying assumptions.** Before we explain how we extend the model from [38] to incorporate memory effects, we comment on its main simplifying assumptions. At present, our model does not include any information on local flow rate (apart from information about the distance to the previous bifurcation); a more realistic model for the CFL recovery should include such information. Furthermore, the current model is two-dimensional. These simplifying assumptions could easily be relaxed in future work. For instance, in three dimensions, one needs to account for the angle defined by the planes containing the current and previous bifurcation in the model. Therefore, the model presented here should be viewed as a first attempt to account for the effects of CFL disruption in HS.

**Rewriting of the model.** In this section, we rewrite the HS model with memory effects ((2) from the main text) in terms of haematocrit levels  $H$  and flow rates  $Q$  experienced by the vessels belonging to a given bifurcation ((3) from the main text). The definitions of  $FQ_{E,f}$  and  $FQ_{B,f}$  can be written as:

$$FQ_{E,f} = \frac{Q_f H_f}{Q_P H_P}, \quad FQ_{B,f} = \frac{Q_f}{Q_P}.$$

Substituting these expressions into (2) from the main text gives:

$$\text{logit} \left( \frac{Q_f H_f}{Q_P H_P} \right) = A_f + B \text{logit} \left( \frac{Q_f/Q_P - X_{0,f}}{1 - X_{0,u} - X_{0,f}} \right).$$

Recalling that  $\text{logit}(x) = \ln(x/(1-x))$ , we have

$$\ln \left( \frac{Q_f H_f}{Q_P H_P - Q_f H_f} \right) = A_f + B \ln \left( \frac{Q_f - X_{0,f} Q_P}{Q_P - Q_f - X_{0,u} Q_P} \right).$$

Appealing to conservation of blood (overall)

$$Q_P = Q_f + Q_u$$

and RBCs (in particular)

$$Q_P H_P = Q_f H_f + Q_u H_u \quad (\text{S.17})$$

at diverging bifurcations, we arrive at

$$\ln \left( \frac{Q_f H_f}{Q_u H_u} \right) = A_f + B \ln \left( \frac{Q_f - X_{0,f} Q_P}{Q_u - X_{0,u} Q_P} \right).$$

This equation can also be written as

$$\ln\left(\frac{H_f}{H_u}\right) = A_f + B \ln\left(\frac{Q_f - X_{0,f}Q_P}{Q_u - X_{0,u}Q_P}\right) - \ln\left(\frac{Q_f}{Q_u}\right),$$

which yields

$$\frac{H_f}{H_u} = e^{A_f} \times \left(\frac{Q_f - X_{0,f}Q_P}{Q_u - X_{0,u}Q_P}\right)^B \times \frac{Q_u}{Q_f}.$$

**Choice of parameter values and CFL recovery function.** Here we introduce the functional forms for  $A_f$ ,  $X_{0,f}$  and  $X_{0,u}$ , using empirical data to justify our choices. Guided by the dependence of  $A$  on the network branching history described in [15] (see Figure 7 therein), we propose

$$A_f = A + A_{shift}f(l; d_P), \quad (\text{S.18})$$

where  $A$  is given in (S.14), the positive constant  $A_{shift}$  corresponds to the maximum CFL disruption effect, and the function  $f(l; d_P)$  describes how the recovery of the CFL depends on the distance  $l$  to the previous bifurcation and the diameter  $d_P$  of the parent vessel<sup>3</sup>.

For parameter  $A$ , we only have access to the scattered data with respect to the regressor from [53] (as opposed to the regressor from [38]), which reads

$$A = -6.96 \ln\left(\frac{d_\alpha}{d_\beta}\right)/d_P. \quad (\text{S.19})$$

Using the extreme values of  $A$  in these data (see Supplementary Figure S8c), we estimate  $A_{shift} = 0.5$ . Note that in branching networks with every pair of daughter vessels having equal radii, both [53] and [38] yield  $A = 0$ . Thus, for our networks, the choice of  $A$  does not affect  $A_f$  at all (see (S.18)).

For simplicity, we model the CFL recovery using an exponential function

$$f(l; d_P) = e^{-\frac{l}{\omega d_P}}, \quad (\text{S.20})$$

where  $\omega$  controls the temporal dynamics of CFL recovery. From [32], we note that the CFL width is (approximately) 90% recovered at a distance  $l_{90} = 10d_P$  from the previous bifurcation (see also Figure 2g). Accordingly, we choose  $\omega$  so that

$$0.1 = e^{-\frac{10}{\omega}} \implies \omega = \frac{10}{\ln(10)} \approx 4.$$

Guided by the dependence of  $X_{0,f}$  on flow history described in [15], we propose

$$X_{0,f} = X_0(1 - f(l; d_P)). \quad (\text{S.21})$$

Assuming, as a first approximation, that  $X_{0,f} + X_{0,u}$  is constant and independent of the distance to the previous bifurcation (see Figure 2g), we define

$$X_{0,u} = X_0(1 + f(l; d_P)). \quad (\text{S.22})$$

---

<sup>3</sup>Consistency of the model requires that  $A_u = A - A_{shift}f(l; d_P)$ .



### A.5.3 Validation of the HS model with memory

We validate the HS model with memory by comparing its predictions with results from the RBC simulations in the double-t geometry. We assume that all vessels have the same diameter ( $d = 33 \mu\text{m}$ ), and that the flow rate splits evenly at both bifurcations. If we assume further that the CFL is fully established at the network inlet vessel,  $H_{inlet} = 20\%$ , then (1) from the main text supplies  $H_1 = H_2 = H_{inlet} = 20\%$ . We use conservation of RBCs ((S.17)) and the new HS model ((3)) from the main text to estimate haematocrit values in the unfavourable and favourable daughter branches after the second bifurcation (channels 3 and 4, respectively) for varying inter-bifurcation distances  $\delta$ . The results are summarised in Supplementary Table S9. For  $\delta = 4d$ , the new HS model predicts haematocrits within 5% of the values calculated from RBC simulations. Given the uncertainty in determining discharge haematocrit in the RBC simulations and given that the new model neglects effects due to asymmetric streamline splitting [37], we conclude that our new model provides a good, leading-order approximation to the effects of CFL disruption on HS.

Finally, we compare the CFL evolution dynamics calculated from the RBC simulations (for  $\theta = 0$  and  $\theta = \pi$ ) with those predicted from the proposed evolution of  $X_{0,f}$  and  $X_{0,u}$  ((S.21) and (S.22)). In the absence of a known functional form relating the CFL width  $W$  and the minimum flow fraction  $X_0$ , we define

$$X_{0,f/u} = \frac{W_{f/u}}{d_P}. \quad (\text{S.23})$$

(S.23) is based on the diagram in Supplementary Figure S8a and the assumptions of a cross-sectionally uniform velocity profile within a one-dimensional vessel cross-section. Combining (S.16), (S.23), (S.21) and (S.22), we conclude

$$W_{f/u} = d_P X_{0,f/u} = d_P X_0 (1 \mp f(l, d_P)) = 0.964 \times (1 - H_P) \left(1 \mp e^{-\frac{l}{4 \times d_P}}\right). \quad (\text{S.24})$$

We remark that for a well-established CFL (i.e.  $l \rightarrow \infty$ ), (S.24) predicts (noting that channel 1 serves as the parent vessel for the second bifurcation and estimating  $H_P = 0.2$  from Supplementary Table S6) a CFL width of about  $0.77 \mu\text{m}$ , whereas our RBC simulation predicts a value of approximately  $1.8 \mu\text{m}$  (see Supplementary Figure S8b). We postulate that this discrepancy is caused by our oversimplification of the relationship between the CFL width and the minimum flow fraction ((S.23)). Nevertheless, we can adjust (S.24) so that it is consistent with the established CFL width of  $1.8 \mu\text{m}$  by writing

$$W_{f/u} = 1.8 \times \left(1 \mp e^{-\frac{l}{4 \times d_P}}\right). \quad (\text{S.25})$$

In this case the CFL evolution (for  $\theta = 0$  and  $\theta = \pi$ ) follows a trend similar to that observed in our RBC simulations (Supplementary Figure S8b). In particular, our assumption that  $l_{90} = 10d_P$  is in good agreement with our simulation results (see dashed line in Supplementary Figure S8b).

## A.6 Explanation of higher mean oxygen values for small $\lambda$

We observed that CFL disruption effects increase the mean oxygen concentration in the chosen network (Supplementary Figure S6). Here, we provide an explanation of this phenomenon.

We define

$$\Delta_\alpha H = H_\alpha - H_P, \quad \Delta_\beta H = H_\beta - H_P, \quad (\text{S.26})$$

where  $P$  is the parent branch and  $\alpha$  and  $\beta$  are the daughter branches of any diverging bifurcation. Conservation of blood and RBCs at this bifurcation then yields

$$Q_\alpha + Q_\beta = Q_P \quad (\text{S.27})$$

$$Q_\alpha (H_P + \Delta_\alpha H) + Q_\beta (H_P + \Delta_\beta H) = Q_P H_P. \quad (\text{S.28})$$

Combining (S.28) and (S.27) supplies

$$\frac{Q_\alpha}{Q_\beta} = -\frac{\Delta_\beta H}{\Delta_\alpha H}. \quad (\text{S.29})$$

We deduce that, at diverging bifurcations, the haematocrit level in the daughter branch with higher flow rate deviates less (in absolute value) from the haematocrit in the parent vessel than the branch with lower flow rate.

We note further that all paths connecting the inlet and outlet vessels in the direction of blood flow in a given network are topologically and geometrically equivalent. Therefore, heterogeneity in haematocrit splitting arises solely from CFL disruption effects. If haematocrit is elevated in one of the daughter branches, its impedance will increase, and, as a result, it will receive a lower flow rate.

Combining these two effects, we see that, in the chosen networks, haemoconcentration in any daughter branch is more significant than haemodilution in its sibling. As a consequence, and given that the strength of the oxygen source term in (S.13) is a linear function of  $H$ , we observe higher mean oxygen levels when the effects of CFL disruption are taken into account (especially for small  $\lambda$ ). Future work will investigate this effect by making source term a function of RBC mass flux (*i.e.*  $QH$ ) or relaxing the assumption that the RBCs have infinite oxygen carrying capacity.

## B Supplementary tables/figures

Supplementary figures and tables supporting the main manuscript text and supplementary information:

- Supplementary Tables S1–S9.
- Supplementary Figures S1–S8

Table S1: Average vessel lengths and diameters reported in a variety of tissues under physiological conditions.

Animal (tissue)	Vessel type	$\bar{L}(\mu\text{m})$	$\bar{d}(\mu\text{m})$	$\lambda = \bar{L}/\bar{d}$	Reference
Wistar Kyoto Rat (mesentery)	Arteriole	337.0	13.2	25.5	[65, 66]
	Capillary	424.0	8.7	48.7	[65, 66]
	Venule	334.0	20.6	16.2	[65, 66]
Myotis Bat (wing)	Arteriole	206.0	7.0	29.4	[67]
	Capillary	74.0	3.7	20.0	[68]
	Venule	200.0	21.0	9.5	[68]
Cat (sartorius muscle)	Arteriole	96.0	7.4	13.0	[69]
	Venule	68.0	6.8	10.0	[70]
Golden Hamster (retractor muscle)	Arteriole	101.2	5.7	17.8	[71]
	Venule	57.7	3.6	16.0	[71]
Human	Capillary	350.0	5.0	70.0	[72]

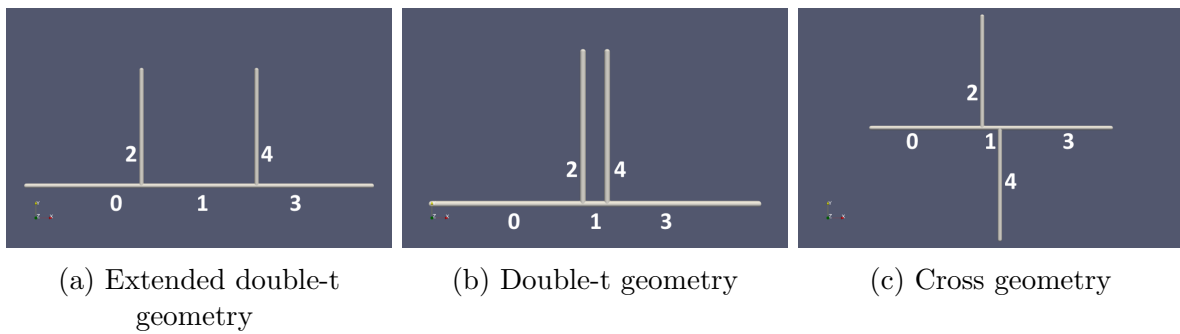


Figure S1: Computational domains considered showing the numbering of the different channels in the network: (a) extended double-t geometry, (b) double-t geometry, (c) cross geometry.

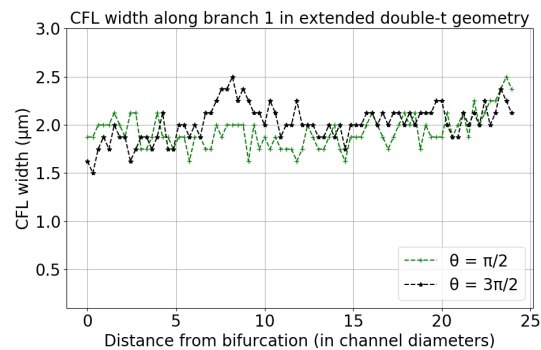


Figure S2: CFL channel 1 double-t geometry perpendicular to bifurcation planes.

Table S2: Previous studies reporting morphological or haemodynamic changes following vascular normalisation therapy.

Ref.	Model	Treatment	Changes reported	$\lambda$ ratio implications	Efficacy
[73]	MDA-MB-361HK tumour model	Herceptin	Reduced vessel diameter, unchanged length	$\lambda$ increase	Tumour growth slowed and increased survival
[74]	Shionogi tumour model	Androgen withdrawal	Reduced vessel diameter	Possible $\lambda$ increase	Tumour regression followed by relapse
[41]	Glioblastoma tumour model	Cediranib	Transient reduction in vessel diameter and haemoglobin concentration	Possible $\lambda$ increase	Increased survival
[75]	Rip-Tag2 tumour model	Anti- $\alpha 6$ integrin antibody	Reduced vessel diameter	Possible $\lambda$ increase	Impaired tumour angiogenesis
[45]	Murine mammary carcinoma MCAIV	DC101	Relatively higher reduction in diameter than in length	$\lambda$ increase	Increased drug penetration via functional normalisation
[76]	LS174T tumour model	Anti-VGF antibody (A4.6.1)	Reduced vessel diameter, unchanged length	$\lambda$ increase	Vascular regression and decreased permeability

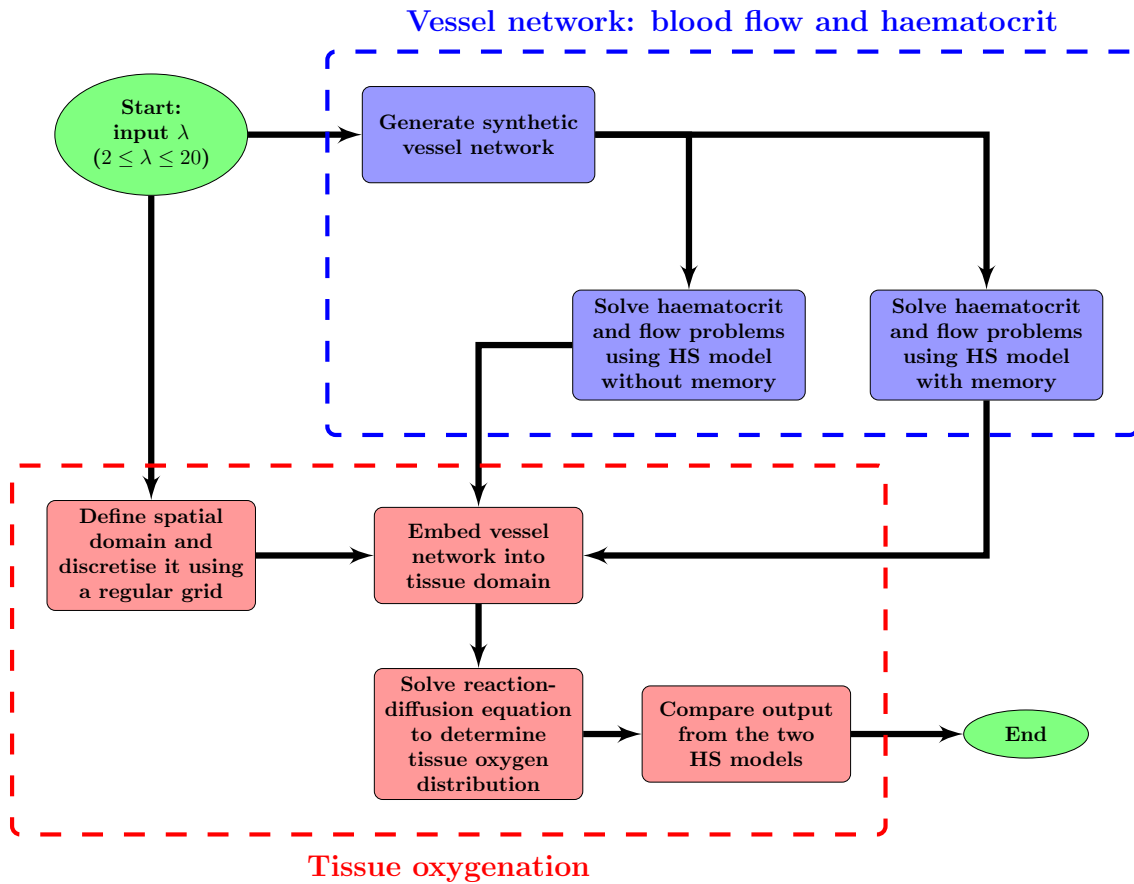
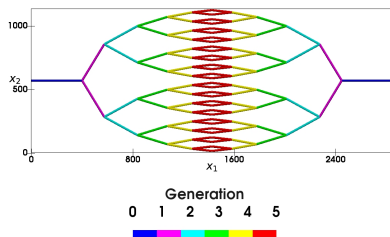


Figure S3: Flow chart summarising the main components of our hybrid model for tissue oxygen perfusion, as implemented within Microvessel Chaste (see [20]).

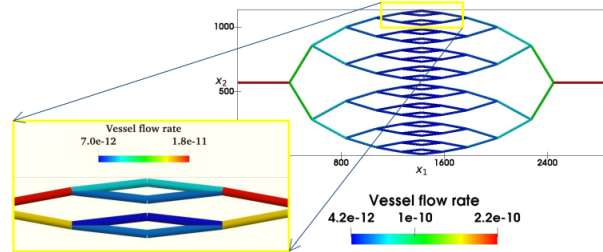
Table S3:  $\lambda$  values measured in MC38 tumours following DC101 treatment over time.

Day	Mouse 1	Mouse 2	Mouse 3	Mouse 4	Mouse 5
0	4.532	4.065	4.141	4.122	4.054
1	5.301	4.098	4.336	4.432	3.878
2	6.222	4.429	4.396	5	4.756
3	5.382	4.465	3.89	5.353	5.068
4	4.395	4.418	3.273	6.342	4.237

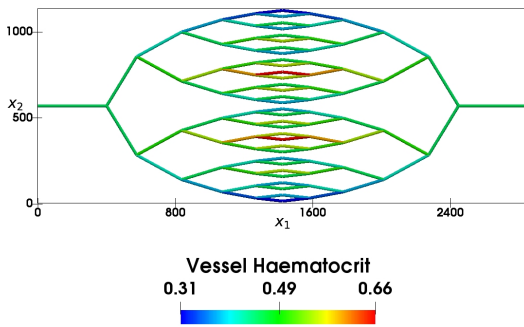




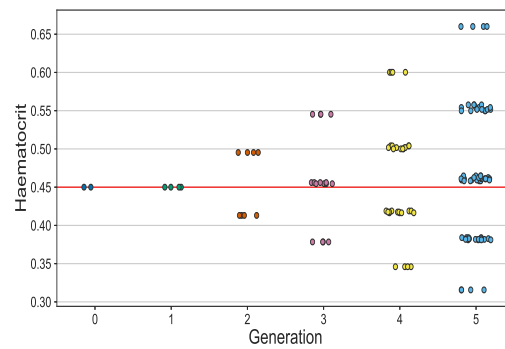
(a) A typical forking vessel network



(b) Vessel flow rates (in  $\text{m}^3/\text{s}$ )

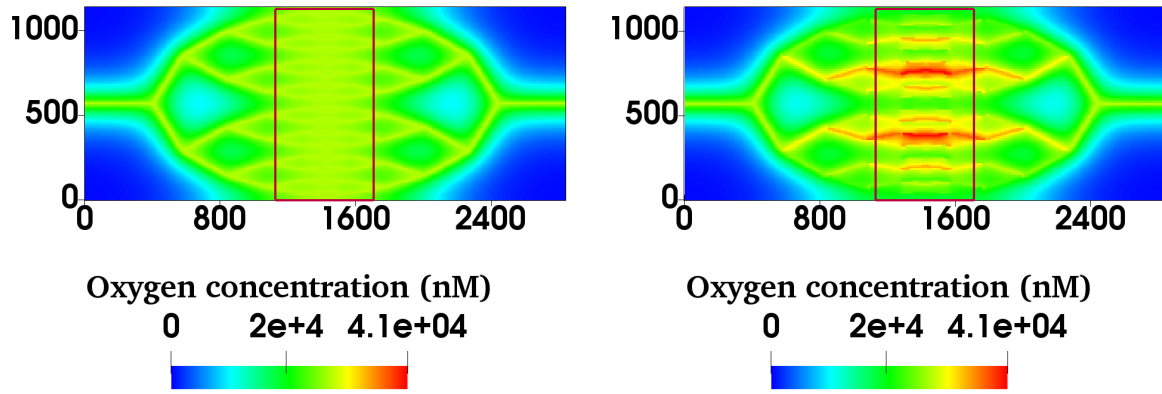


(c) Distribution of haematocrit across vessel network (model with memory effects)



(d) Propagation of memory effects

Figure S4: (a) A typical symmetric forking network with 6 generations of vessels. (b) Flow rates almost halve between consecutive vessel generations. However, small differences in flow rates between daughter vessels arise due to non-uniform haematocrit splitting (HS), as can be observed in the inset (note that the range of the colour bar has been adjusted to represent only the selected vessels). (c) Differences in the predicted haematocrit levels of daughter vessels (within a single vessel generation) become more pronounced as the generation number increases. (d) For the new HS model, the haematocrit distribution becomes more disperse as the number of bifurcations included in the network increases (the red horizontal line represents the predicted haematocrit when memory effects are neglected and haematocrit is distributed uniformly across the network). Each circle corresponds to a single vessel and different colours correspond to different vessel generations.



(a)  $\lambda = 4$ , model without memory effects

(b)  $\lambda = 4$ , model with memory effects

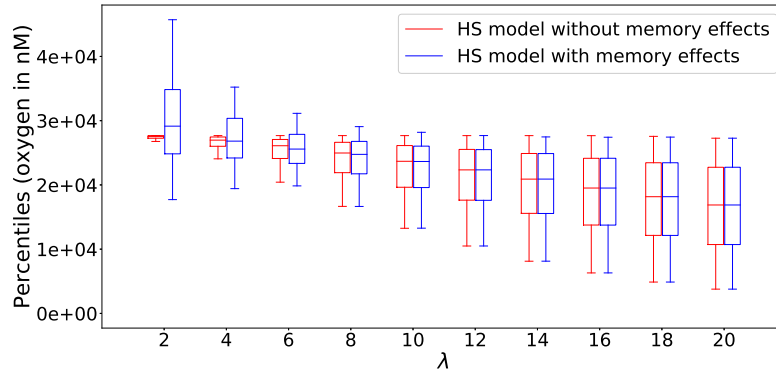
Figure S5: For  $\lambda = 4.0$ , the model with memory effects yields more pronounced oxygen heterogeneity (*i.e.* more dispersed oxygen distribution) in the region of interest bounded by red rectangles in (a) and (b) (note that the spatial scales are in microns).

Table S4: Timecourse of Pearson's r-values calculated for different mice at different days of measurement implanted with the MC38 cell line. Day 0 corresponds to the day of the first measurement, when the tumour reached a specified size (4mm in diameter; see the main text). The corresponding values of  $\bar{L}$ ,  $\bar{d}$  and  $\lambda$  are reported in the main text (see Table 1). The missing datum for tumour 3 on Day 3 is due to the laser on the microscope failing during imaging.

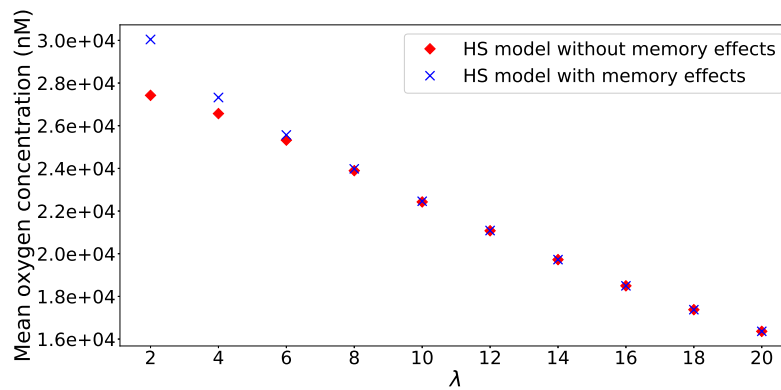
Day	1	2	3	4	5	6
0	0.05	-0.06	-0.07	0.10	-0.13	0.00
1	0.03	-0.05	-0.07	-0.07	-0.13	-0.00
2	-0.08	-0.07	-0.06	-0.17	-0.19	0.02
3	-0.09	-0.09	-	-0.14	-0.13	-0.02
4	-0.14	-0.11	-0.08	-0.17	-0.12	-0.07
5	-	-0.09	-	-	-0.07	-0.11
6	-	-0.04	-	-	-	-
7	-	-0.08	-	-	-	-

Table S5: Timecourse of Pearson's r-values for mice implanted with the B16F10 and LLC cell lines. Day 0 corresponds to the day of the first measurement, when the tumour reached a specified size (4mm in diameter; see the main text). The corresponding values of  $\bar{L}$ ,  $\bar{d}$  and  $\lambda$  are reported in the main text (see Table 1).

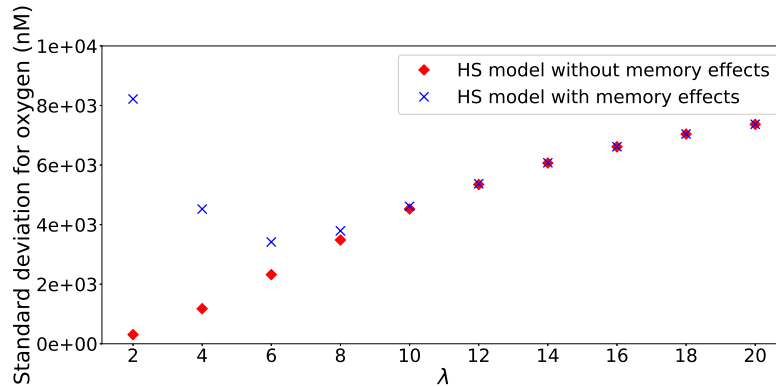
Day	B16F10			LLC
	1	2	3	
0	-0.08	-0.08	-0.06	0.03
1	-0.05	-0.06	-0.09	0.02
2	-0.05	-0.12	-0.06	-
3	-0.03	-0.11	-0.06	-
4	-	-	-0.06	-
5	-	-	-0.05	-



(a) Boxplots showing tissue oxygen concentration distribution as a function of  $\lambda$



(b) Mean oxygen concentration as a function of  $\lambda$



(c) Standard deviation (oxygen) as a function of  $\lambda$

Figure S6: Summary statistics illustrating how for a vessel network with 6 generations its  $\lambda$  value and the HS model affect tissue oxygenation. (a) Boxplots showing how the tissue oxygen distribution changes as  $\lambda$  varies for the two different HS rules. (b) Mean oxygen concentration increases as  $\lambda$  decreases (and the vessel density increases). (c) Standard deviation in the tissue oxygen concentration increases with  $\lambda$  when memory effects are neglected ((1) from the main text). When memory effects are considered ((2) from the main text), the standard deviation increases for small  $\lambda$  values. The mean and standard deviation for the two models converge for large  $\lambda$  values. Model parameter values as per Supplementary Table S8.

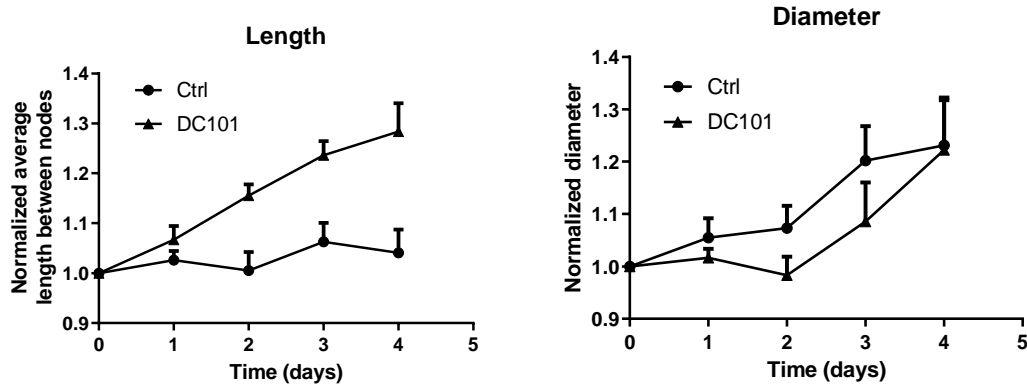


Figure S7: Vessel length and diameter in MC38 tumours over time following DC101 treatment compared with control (n=5).

Table S6: Parameters in RBC simulations in synthetic capillary networks

Parameter	Description	Value	Reference
$d$	Cylindrical channel diameter	$33 \mu\text{m}$	Current study
$L'$	Inlet/outlet channel length	$25d$	[32]
$\delta$	Distance between branching points	$4d, 25d$	[32], current study
$\bar{v}_{inlet}$	Inlet mean velocity	$600 \mu\text{m/s}$	[9]
$H_{inlet}$	Inlet discharge haematocrit	20%	[9]

Table S7: Parameters used in RBC simulation algorithm. The number of faces is chosen in such a way that the average edge length of a triangular element matches the grid spacing of the fluid lattice. The value of the capillary number is representative of typical flows in the microcirculation. The adopted value of the Föppl-von Kármán number matches the intrinsic property of healthy RBC membranes. The remaining moduli are chosen in such a way that the local area, total surface area and volume of the RBCs are constrained within a few percent while simulations remain numerically stable.

Parameter	Description	Value	Unit	Comment
$N_f$	Number of faces	500	-	See mesh convergence analysis in [33]
$r_{RBC}$	RBC diameter	8	$\mu\text{m}$	6.2–8.2 $\mu\text{m}$ physiological range
$\eta$	Plasma viscosity	1	mPa s	Approximated by water
$Ca$	Capillary number	0.1	-	$Ca = \frac{\eta \dot{\gamma}_{RBC}}{\kappa_s}$ , $\dot{\gamma} = \frac{\bar{v}_{inlet}}{d}$ (see Suppl. Table S6, [32])
$\Gamma$	Föppl-von Kármán no.	400	-	$\Gamma = \frac{\kappa_s r_{RBC}^2}{\kappa_B}$
$\kappa_\alpha$	Dilation modulus	0.5	-	Strong volume and area conservation
$\kappa_A$	Surface area modulus	1	-	Strong volume and area conservation
$\kappa_V$	Volume modulus	1	-	Strong volume and area conservation

Table S8: Parameters used to simulate tissue oxygen.

Parameter	Description	Value	Unit	Reference
$D$	Diffusivity	0.00145	$\text{cm}^2 \text{min}^{-1}$	[77]
$\kappa$	Consumption rate	13.0	$\text{min}^{-1}$	[77]
$\gamma$	Vessel permeability	6.0	$\text{cm min}^{-1}$	[77]
$c_{stp}$	Ideal gas concentration	$\frac{1}{0.0224}$	$\text{mol m}^{-3}$	[78]
$p_{ref}$	Reference partial pressure	20	mmHg	[77]
$\alpha_{eff}$	Volumetric solubility	$3.1 \times 10^{-5}$	$\text{mmHg}^{-1}$	[64]
$H_{inlet}$	Inlet haematocrit	0.45	-	[79]
$d_{inlet}$	Diameter of inlet vessel	100	$\mu\text{m}$	Estimated from [52]
$A_{shift}$	Maximum CFL disruption effect	0.5	-	Estimated here
$\omega$	Temporal dynamics of CFL recovery	4	-	Estimated here
$\mu_p$	Plasma viscosity	$10^{-3}$	Poiseuille	Similar to [77]
$p_{in}$	Inlet pressure	$3.32 \times 10^3$	Pa	Similar to [77]
$p_{out}$	Outlet pressure	$2.09 \times 10^3$	Pa	Similar to [77]

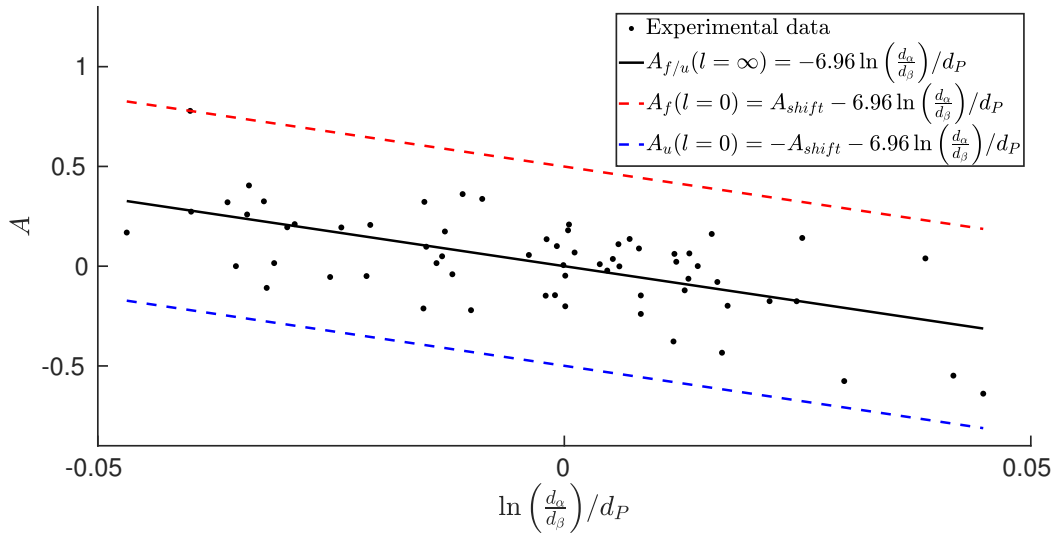
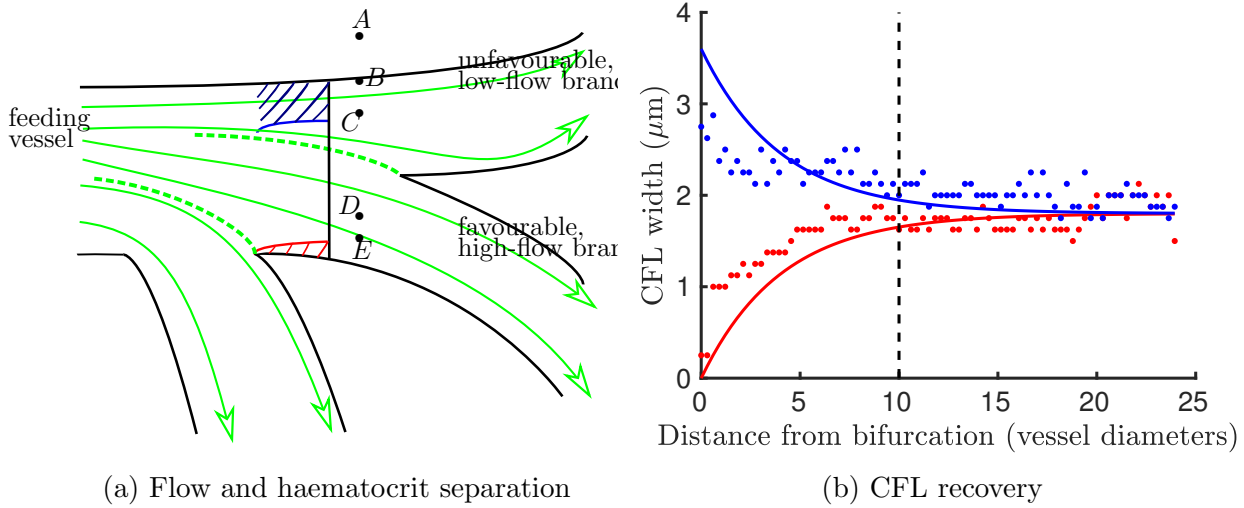


Figure S8: (a) A schematic diagram presenting the geometric intuition behind (blood) flow and haematocrit separation illustrate why two distinct minimum-flow fractions are needed to characterise the favourable and the unfavourable branches:  $\|AB\| = X_{0,u}$ ,  $\|DE\| = X_{0,f}$ ,  $\|AC\| = FQ_{B,u}$  and  $\|CE\| = FQ_{B,f}$ . Blood flow separation at the two consecutive bifurcations is shown in dotted green, streamlines are sketched with yellow curved arrows, and the CFL recovery on the favourable (unfavourable) side of the parent vessel after the first bifurcation is sketched in red (blue). Whenever  $FQ_{B,f} < X_{0,f}$  ( $FQ_{B,u} < X_{0,u}$ ), the favourable (unfavourable) branch only draws blood from the CFL and it thus receives pure plasma. (b) Model of CFL recovery as described by (S.25) shows similar trends to and is in satisfactory agreement with the CFL width data from RBC simulations in Figure 2g (given the simplifying assumptions). The established CFL width of  $1.8 \mu\text{m}$  chosen by inspection for this particular dataset. (c) Dispersion of values for  $A$  (reproduced using Figure 6 from [15]) is used with the regression from [53] to estimate the value of  $A_{shift} \approx 0.5$  in (S.18), based on deviation from the regression. We assume the CFL disruption to be the primarily cause of this deviation, and thus its maximum (absolute) value should correspond to  $l = 0$  in (S.20) (i.e.  $f = 1$  in (S.18)).



Table S9: Haematocrits predicted by the model with CFL memory effects

Distance	$H_{inlet}$	$H_u$	$H_f$
$\delta = 4d$	20.0	17.7	22.3
$\delta = 11d$	20.0	19.6	20.4
$\delta = 18d$	20.0	19.9	20.1
$\delta = 25d$	20.0	20.0	20.0